Composite Structures 292 (2022) 115582

Contents lists available at ScienceDirect

Composite Structures

journal homepage: www.elsevier.com/locate/compstruct

Modified couple stress theory application to analyze mechanical buckling behavior of three-layer rectangular microplates with honeycomb core and piezoelectric face sheets

Chunwei Zhang [a,b,*], Arameh Eyvazian [b,c,*], Mohammad Alkhedher [d], Mamdooh Alwetaishi [e], N. Ameer Ahammad [f]

[a] State Key Laboratory of Precision Blasting, Jianghan University, Wuhan 430056, China
[b] Multidisciplinary Center for Infrastructure Engineering, Shenyang University of Technology, Shenyang 110870, China
[c] Department of Mechanical Engineering, Politecnico di Milano, Via La Masa 1, 20156 2 Milan, Italy
[d] Mechanical Engineering Department, Abu Dhabi University, United Arab Emirates
[e] Department of Civil Engineering, College of Engineering, Taif University, P.O. Box 11099, Taif 21944, Saudi Arabia
[f] Department of Mathematics, Faculty of Science, University of Tabuk, P.O. Box741, Tabuk 71491, Saudi Arabia

ARTICLE INFO

Keywords:
Mechanical buckling
Honeycomb structures
Piezoelectric materials
Sandwich microplate
Modified couple stress theory
Sinusoidal shear deformation theory

ABSTRACT

The current study is aimed to analyze the mechanical buckling of a three-layered microplate made from honeycomb structures sandwiched between two piezoelectric face sheets. The microplate is located on an elastic foundation that stands both normal and shearing loads. Minghui and Jiuren relations were employed to determine the effective mechanical properties of the honeycomb core. The sinusoidal shear deformation theory (SSDT) was also employed as a higher-order theory with trigonometric shear deformation function to describe the displacement components. The governing equations were derived using the virtual displacement principle and modified couple stress theory (MCST) was employed to predict the results in micro dimension. Navier's solution method was chosen to analytically extract the critical buckling loads for a simply supported edges microplate. The effect of the most important parameters such as geometrical specifications of the honeycomb core on the results was also considered and discussed. Nowadays the honeycomb structures are widely used in different areas of sciences and technologies due to their lightweight and high stiffness. Also, the piezoelectric materials are applied as sensors and actuators in smart engineering structures. Therefore, the outcomes of this study may help in designing and manufacturing more applicable structures and smart devices capable of tolerating loading conditions, especially in small dimensions.

1. Introduction

Honeycomb structures are usually characterized by their high stiffness and low density. These structures can be employed in engineering structures and industries that have both weight and stiffness limitations. Honeycombs are usually applied with reinforcement layers on their surfaces [1]. Aerospace engineering and aircrafts industry are the most well-known areas of honeycomb structures applications [2]. Although honeycomb structures have great potential in different fields, their mechanical responses have not been extensively discussed. To determine the effective values of elasticity moduli, density, and Poisson's ratio of the honeycomb structures Gibson *et al.* [3] presented the first formulations which were further modified by Minghui, and Jiuren [4]. Yu and Cleghorn [5] employed the classical, first-order, and third-order shear deformation theories to analyze the free vibration of honeycomb panels. They determined the mechanical properties of the structure using Gibson and Ashby formulations. Maheri and Adams [6] studied the flexural vibration damping of sandwiched honeycomb beams. They used Nomex and Aluminum in the honeycomb core and integrated them with two faces. Later, the vibration and sound propagation of the honeycomb core sandwich beam from truss were analyzed by Ruzzene [7].

The sandwich structures are composed of three layers in which the mid-layer is thicker but softer than the faces. The mid-layer is also known as the core. Using the sandwich structures helps in reaching the desired behaviors against different loading conditions making them more applicable in various fields of science and technology [8–13].

* Corresponding authors.
E-mail addresses: zhangchunwei@sut.edu.cn (C. Zhang), arameh.eyvazian@polimi.it (A. Eyvazian).

https://doi.org/10.1016/j.compstruct.2022.115582
Received 1 August 2021; Received in revised form 31 March 2022; Accepted 8 April 2022
Available online 20 April 2022
0263-8223/

Consequently, these structures have been widely explored to find out their different bending, buckling, and vibration responses. The main part of designing and analyzing the sandwich structures is the proper selection of the material types. The faces are usually used to integrate the core, which cannot be used alone. The honeycombs are suggested to be used as the core of sandwich structures. Reviewing the literature showed that the size of the cells can affect the vibrational behavior of sandwich three-layered beams as presented by Dai and Zhang [14]. They used the finite element method to extract the results and concluded that the cell size is an important parameter characterizing the cellular core rigidities influencing the vibration responses. Hajmohammad *et al.* [15] addressed the dynamic response of visco-sandwich plates with auxetic honeycombs core. Their structure was subjected to blast and magnetic field loads and differential cubature and Newmark methods were used to solve the equations. Cheng *et al.* [16] employed a refined sandwich beam theory to explore the free vibrational behavior fiber-reinforced honeycomb sandwich beams. Hamilton's principle was used to extract the equations, which were solved by the Ritz method. Their results were compared with Timoshenko and higher-order beams theories that led to the proper agreement. Subramani *et al.* [17] used higher-order shear deformation theory for the vibration analysis of sandwich beams with a honeycomb core, and carbon fiber-reinforced laminated composite skins. They solved the equations via the finite element method. Yongqiang and Dawei [18] used improved Reddy's third-order theory to provide a parabolic distribution of the transverse shear stress along the thickness direction to investigate the flexural vibration of honeycomb panels and compared the results with the experimental and finite element data. An experiment was conducted on the dynamic response of a sandwich beam with honeycomb core and carbon/epoxy composite skins which were filled with magnetorheological fluids by Eloy *et al.* [19]. Nonlinear primary resonance of rectangular honeycomb sandwich panels was analyzed with the aid of the homotopy method by Li *et al.* [20]. Their study was based on Reddy's shear deformation theory and used the Galerkin method to reduce the nonlinear partial differential equations into nonlinear ordinary differential equations. Wang *et al.* [21] investigated the vibration characteristics of sandwich panels with a hierarchical composite honeycomb core. They compared the vibration characteristics of the panel with a hierarchical cross-honeycomb sandwich core with those of a panel with a hierarchical square-honeycomb sandwich core.

Piezoelectric materials are an advanced and smart class of materials that react to the electro-mechanical loadings [22,23]. These materials react to electrical or mechanical loads due to their direct and converse effects, respectively [24]. Smart materials are used to control the behavior of the structures [25]. These materials can be used as a primary structure, integrators, sensors, or actuators. The piezoelectric materials and their mechanical behaviors have been extensively explored [26–32]. Active vibration control of functionally graded (FG) piezoelectric plate was addressed by Li *et al.* [33]. They used classical plate theory to extract the equations of motion, which were solved by the Rayleigh-Ritz method. They studied the effect of external voltage position on active vibration control under the non-uniform electric field. Two piezoelectric patches served as actuators and were integrated into a porous circular plate in a study by Arshid and Khorshidvand [34]. They considered the effect of the applied voltage to the piezoelectric faces on the natural frequencies of the structure. Duc *et al.* [35] used the first-order shear deformation theory to show the nonlinear dynamic response and vibration of the piezoelectric FGM plates under thermal load. Large-amplitude vibration of reinforced composite annular plates with integrated piezoelectric layers on an elastic foundation was assessed by Keleshteri *et al.* [36]. Abad and Rouzegar [37] examined an FG rectangular plate including two piezoelectric layers attached to its top and bottom surfaces, and presented its vibrational behavior.

In order to analyze the structures such as beams, plates, and shells, there are different kinds of theories that in some of them, the shear deformation effects are neglected [38–41], but in the others, they are taken into account using different shear deformation functions [42–50]. For example, classical plates theory which is based on Kirchhoff's assumptions neglects the shear deformation effects and therefore, the derived equations based on it are simpler; accordingly, the obtained results also have some errors due to neglecting these effects. The first-order and higher-order shear deformation theories such as third-order, trigonometric, and quasi-3D ones are recently used by the authors due to their more accuracy and reliability which leads to obtaining more complex equations and also, more near-to-real results [51–56]. In these theories, the shear deformation effects are regarded and it causes that the obtained results be closer to the experimental ones. Becheri *et al.* [57] presented an exact analytical solution for mechanical buckling analysis of symmetrically cross-ply laminated plates including curvature effects. The equilibrium equations were derived according to the refined *n*th-order shear deformation theory. The presented refined *n*th-order shear deformation theory was based on assumption that the in-plane and transverse displacements consist of bending and shear components, in which the bending components do not contribute toward shear forces and, likewise, the shear components do not contribute toward bending moments. Hyperbolic shear deformation theory which as it can be understood from its name, the shear deformation function is a hyperbolic type one, is used by the authors to achieve more accurate results [58–60].

The small-dimension equipment has been quickly developed. Different theories have been also extended to take the size effect into account. The nonlocal elasticity theory was presented for the first time by Eringen [61,62] which became the basis for numerous studies on nanoscale systems [63–65]. A closed-from solutions for thermal buckling analyses of advanced nanoplates according to a hyperbolic four-variable refined theory with small-scale effects presented by Bouazza *et al.* [66]. The shortcomings of this theory for different material types or loading conditions were resolved by the introduction of new theories. The modified versions of couple stress and strain gradient theories, namely modified couple stress theory (MCST) and modified strain gradient theory (MSGT) are some of these theories [67–70]. Farzam and Hassani [71] examined the mechanical behaviors of FG porous microplates, including bending, buckling, and vibrations. They considered the size influence via the MCST, which suggests a material length-scale parameter. MCST was coupled with trigonometric shear deformation theory coupled with isogeometric analysis by Thanh *et al.* [72] who used numerical methods to obtain the results and considered the effect of the small-scale parameter. Vibration and stability analyses of an FG microplate were presented by Bo *et al.* based on MCST [73]. They used Mindlin's assumptions for their kinematic relations. The mechanical and thermal buckling behaviors of a five-layer organic solar cell model were assessed by Li *et al.* [74]. MCST was used by Arefi *et al.* [75] to analyze the thermal buckling of FG rectangular plates, which was reinforced by nanoplatelets in the micro dimension. They discussed the effects of different parameters on the thermal stability of the microplate and compared the results of macro and microstructures.

The literature review shows no research on a sandwich honeycomb structure integrated with piezoelectric patches in small dimensions. Therefore, in this study, Minghui and Jiuren relations are employed to determine the effective mechanical properties of the honeycomb core. The sinusoidal shear deformation theory (SSDT) as a trigonometric higher-order shear deformation theory is employed to describe the displacement components of the microplate. MCST suggests a material length-scale parameter to take into account the size effect. Employing the virtual displacement principle and using a variational approach, the governing equations are derived and solved via the Navier's technique for simply supported boundary type. The effects of different parameters on the critical buckling load are considered and discussed in detail. The current work is the first analysis addressing honeycomb sandwich structures in the micro-scale, hence its results can be regarded as a benchmark for further studies. Designing and manufacturing more applicable engineering structures with the best performance are among

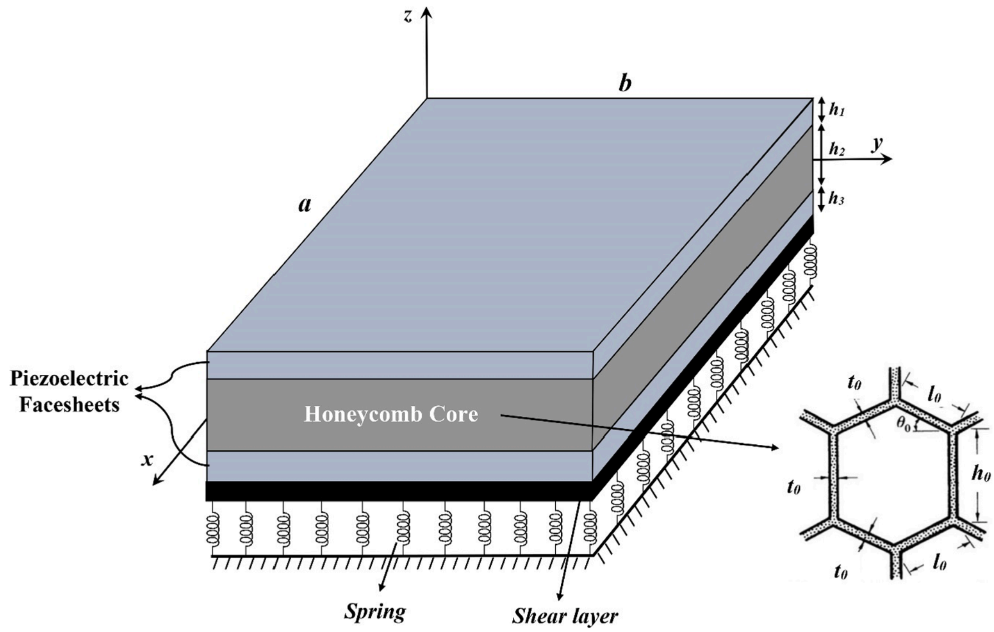

Fig. 1. Schematic of the three-layered microplate with honeycomb core and piezoelectric face sheets.

the other contributions of this work.

2. Basic relations

2.1. Problem definition

A three-layered rectangular microplate with respective length and width of a and b is investigated in this study. The mid-layer of the microplate is made from honeycomb structure, and the top and bottom layers are from piezoelectric materials. h_1, h_2, and h_3 denote the thicknesses of the top, middle, and bottom layers, respectively and the total thickness of the microstructure is their summation as shown by H. The Cartesian coordinate system was employed to analyze the structure whose origin is in the left corner of the mid-plane of the microplate. The microplate was exposed to an electric field located on an elastic foundation including both springs and shear layer. The schematic diagram of the described structure is drawn in Fig. 1.

2.2. Constitutive relations

As mentioned previously, the core of the sandwich microplate is made as a honeycomb structure, which provides both lightweight and high stiffness. Based on the previous studies, the dimensionless effective values of Young's elasticity modulus of in x and y directions can be determined using the following relations [76]:

$$\overline{E}_x = \frac{E_x}{E_H} = \left(1-\gamma_0^2\cot^2\theta_0\right)\frac{\cos\theta_0}{\sin^2\theta_0(\phi_0+\sin\theta_0)}\gamma_0^3, \tag{1}$$

$$\overline{E}_y = \frac{E_y}{E_H} = \left[1-\gamma_0^2\left(\phi_0\sec^2\theta_0+\tan^2\theta_0\right)\right]\frac{\phi_0+\sin\theta_0}{\cos^3\theta_0}\gamma_0^3 \tag{2}$$

Two dimensionless quantities, known as internal aspect ratio (ϕ_0) and dimensionless cell thickness (γ_0), are used in Eqs. (1)-(2) which can be defined as:

$$\phi_0 = h_0/l_0, \gamma_0 = t_0/l_0 \tag{3}$$

where the length of the sides of the hexagonal cell of honeycomb structures is shown by l_0, and their height is shown by h_0. Also, the angle relative to the horizontal level is presented by θ_0, and the cell thickness is t_0. The dimensionless form of the shear moduli can be written as [77]:

$$\overline{G}_{xy} = \frac{G_{xy}}{E_H} = \frac{\phi_0+\sin\theta_0}{(1+2\phi_0)\cos\theta_0}\frac{\gamma_0^3}{\phi_0^2}, \tag{4}$$

$$\overline{G}_{xz} = \frac{G_{xz}}{G_H} = \frac{\cos\theta_0}{\phi_0+\sin\theta_0}\gamma_0, \tag{5}$$

$$\frac{\phi_0+\sin\theta_0}{(1+2\phi_0)\cos\theta_0}\gamma_0 \leqslant \overline{G}_{yz} = \frac{G_{yz}}{G_H} \leqslant \frac{\phi_0+2\sin^2\theta_0}{2(\phi_0+\sin\theta_0)\cos\theta_0}\gamma_0 \tag{6}$$

Note that the average of upper and lower specified values is included for G_{yz} as follow:

$$\overline{G}_{yz} = \frac{\phi_0+\sin\theta_0}{2(1+2\phi_0)\cos\theta_0}\gamma_0 + \frac{\phi_0+2\sin^2\theta_0}{4(\phi_0+\sin\theta_0)\cos\theta_0}\gamma_0 \tag{7}$$

Moreover, the values of Poisson's ratios and dimensionless density may be determined using below relations:

$$\nu_{xy} = \left(1-\gamma_0^2\csc^2\theta_0\right)\frac{\cos^2\theta_0}{\sin\theta_0(\phi_0+\sin\theta_0)}, \tag{8}$$

$$\nu_{yx} = \left[1-\gamma_0^2(1+\phi_0)\sec^2\theta_0\right]\frac{(\phi_0+\sin\theta_0)\sin\theta_0}{\cos^2\theta_0}, \tag{9}$$

$$\overline{\rho} = \frac{\rho}{\rho_H} = \frac{(2+\phi_0)\gamma_0}{2\cos\theta_0(\phi_0+\sin\theta_0)} \tag{10}$$

It is noteworthy that E_H, G_H, and ρ_H are the of Young's modulus, shear modulus, and density of the based material of the honeycomb structure. Furthermore, Then, the stress–strain relations for the honeycomb core can be stated as [78]:

$$\begin{Bmatrix}\sigma_{xx}\\ \sigma_{yy}\\ \sigma_{yz}\\ \sigma_{xz}\\ \sigma_{xy}\end{Bmatrix}^{core} = \begin{bmatrix}Q_{11} & Q_{12} & 0 & 0 & 0\\ Q_{12} & Q_{22} & 0 & 0 & 0\\ 0 & 0 & Q_{44} & 0 & 0\\ 0 & 0 & 0 & Q_{55} & 0\\ 0 & 0 & 0 & 0 & Q_{66}\end{bmatrix}^{core}\begin{Bmatrix}\varepsilon_{xx}\\ \varepsilon_{yy}\\ \gamma_{yz}\\ \gamma_{xz}\\ \gamma_{xy}\end{Bmatrix} \tag{11}$$

where Q_{ij} show the components of the stiffness matrix for the honeycomb core.

The constitutive law for the top and bottom piezoelectric face sheets of the under consideration microplate can be expressed as [79]:

Table 1
Comparing the obtained critical buckling load with those of He *et al.* [95] for an FG microplate based on different parameters changes.

H/l_m	Ref.	$a/H = 5$			$a/H = 10$			$a/H = 20$		
		n								
		0	1	10	0	1	10	0	1	10
∞	He *et al.* [95]	15.3322	6.8611	2.7672	18.0754	7.8276	3.4969	18.9243	8.1142	3.7450
	Present	15.3389	6.8635	2.7600	18.0772	7.8282	3.4937	18.9248	8.1144	3.7441
5	He *et al.* [95]	18.0422	8.3399	3.3619	20.9025	9.3767	4.0513	21.7771	9.6815	4.2752
	Present	18.0513	8.3438	3.3426	20.9048	9.3777	4.0436	21.7777	9.6818	4.2731
2.5	He *et al.* [95]	26.1539	12.7754	5.0407	29.3735	14.0232	5.6631	30.3324	14.3832	5.8505
	Present	26.1707	12.7837	5.0047	29.3776	14.0253	5.6505	30.3334	14.3837	5.8470
5/3	He *et al.* [95]	39.6393	20.1658	7.7001	43.4732	21.7657	8.2906	44.5855	22.2188	8.4589
	Present	39.6695	20.1815	7.6549	43.4805	21.7696	8.2761	44.5873	22.2198	8.4550
5/4	He *et al.* [95]	58.4862	30.5105	11.3322	63.1958	32.6036	11.9349	64.5348	33.1882	12.1011
	Present	58.5353	30.5366	11.2810	63.2079	32.6102	11.9194	64.5378	33.1898	12.0970
1	He *et al.* [95]	82.6938	43.8094	15.9522	88.5416	46.5372	16.6033	90.1804	47.2914	16.7793
	Present	82.7673	43.8488	15.8952	88.5599	46.5471	16.5866	90.1849	47.2938	16.7750

Table 2
Critical buckling load ratio for piezoelectric square microplate based on non-dimensional length-scale parameter values.

	V_0	H/l_m							
		1		2		5		10	
		Present	Jamalpour *et al.* [96]	**Present**	Jamalpour *et al.* [96]	**Present**	Jamalpour *et al.* [96]	**Present**	Jamalpour *et al.* [96]
$l_m = 17.6$ μm	100	1.304512	1.298814	1.103260	1.074704	1.041115	1.011953	1.013514	1.002988
	50	1.305108	1.298922	1.105001	1.074730	1.042815	1.011957	1.014006	1.002989
	0	1.305793	1.299029	1.106592	1.074757	1.043753	1.011961	1.014593	1.002990
	−50	1.306426	1.299136	1.107605	1.074784	1.044639	1.011965	1.015004	1.002991
	−100	1.307017	1.299244	1.108436	1.074810	1.045719	1.011970	1.015647	1.002992
$l_m = 1.76$ μm	100	1.338515	1.296897	1.125008	1.074224	1.044194	1.011876	1.040428	1.002968
	50	1.340037	1.297959	1.129489	1.074489	1.049503	1.011918	1.047538	1.002979
	0	1.346309	1.299029	1.136334	1.074757	1.054437	1.011961	1.051317	1.002990
	−50	1.351170	1.300106	1.142711	1.075026	1.059531	1.012004	1.054821	1.003001
	−100	1.357132	1.301191	1.148906	1.075298	1.064119	1.012047	1.059004	1.003012
$l_m = 0.176$ μm	100	1.314380	1.278998	1.110355	1.069749	1.053329	1.011160	1.050322	1.002789
	50	1.318636	1.288667	1.118302	1.072166	1.058190	1.011546	1.057669	1.002887
	0	1.325590	1.299029	1.126995	1.074757	1.063925	1.011961	1.062320	1.002990
	−50	1.330021	1.310163	1.136418	1.077541	1.068908	1.012406	1.066201	1.003102
	−100	1.337402	1.322159	1.142081	1.080540	1.075778	1.012886	1.701966	1.003222

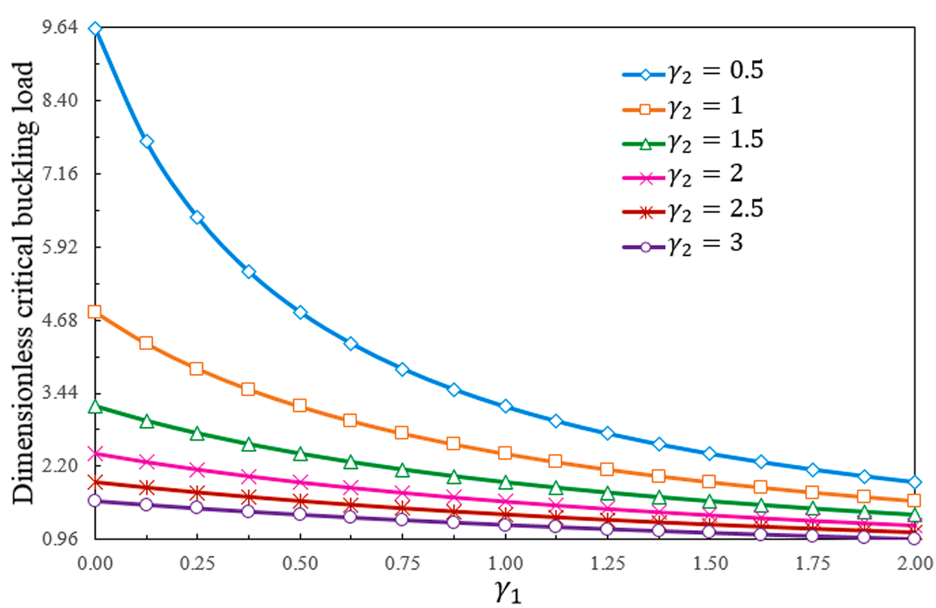

Fig. 2. Effect of loads magnitudes on the dimensionless critical buckling load.

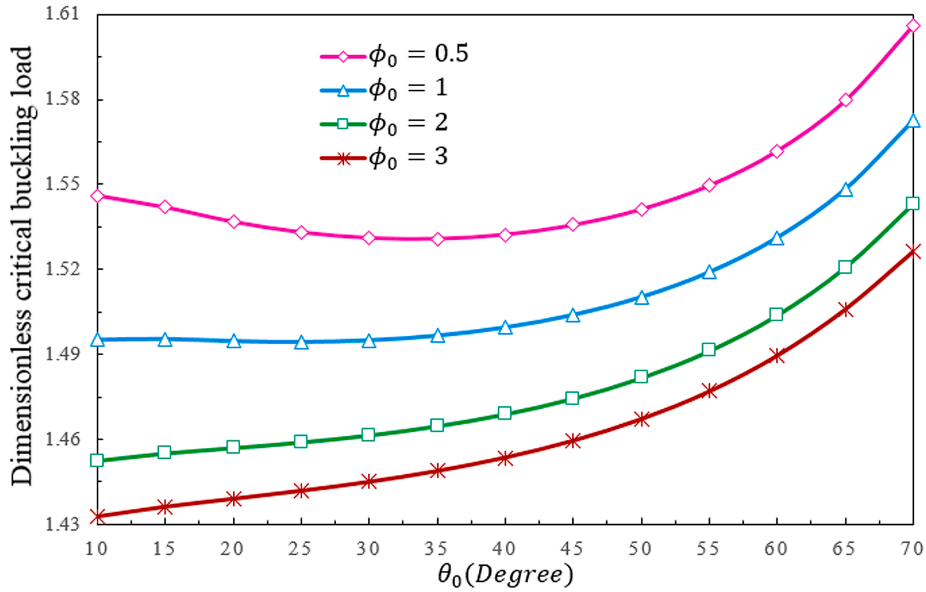

Fig. 3. Influence of internal aspect ratio and angle of honeycomb cells on the dimensionless critical buckling load (Bi-axial).

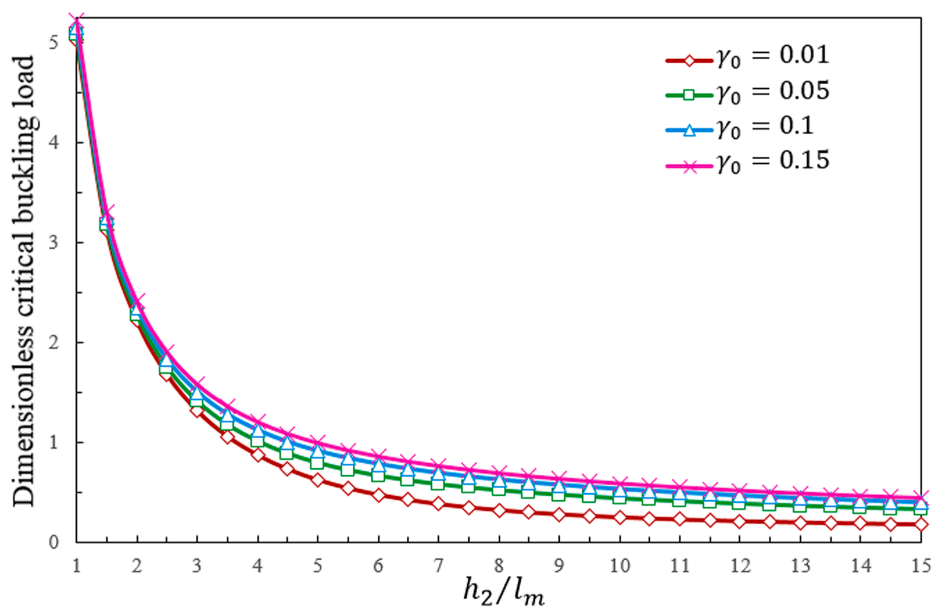

Fig. 4. Dimensionless critical buckling load for various values of core's thickness to length-scale parameter ratio based on different values of dimensionless thickness of honeycomb cells (Bi-axial).

$$\begin{Bmatrix} \sigma_{xx} \\ \sigma_{yy} \\ \sigma_{yz} \\ \sigma_{xz} \\ \sigma_{xy} \end{Bmatrix}^{top,bottom} = \begin{bmatrix} Q_{11} & Q_{12} & 0 & 0 & 0 \\ Q_{12} & Q_{22} & 0 & 0 & 0 \\ 0 & 0 & Q_{44} & 0 & 0 \\ 0 & 0 & 0 & Q_{55} & 0 \\ 0 & 0 & 0 & 0 & Q_{66} \end{bmatrix}^{top,bottom} \begin{Bmatrix} \varepsilon_{xx} \\ \varepsilon_{yy} \\ \gamma_{yz} \\ \gamma_{xz} \\ \gamma_{xy} \end{Bmatrix} - \begin{bmatrix} 0 & 0 & e_{31} \\ 0 & 0 & e_{32} \\ 0 & e_{24} & 0 \\ e_{15} & 0 & 0 \\ 0 & 0 & 0 \end{bmatrix}^{top,bottom} \begin{Bmatrix} E_x \\ E_y \\ E_z \end{Bmatrix} \tag{12}$$

where e_{ij} are the piezoelectric coefficients and E_i are the electric field components.

The electric potential is assumed to vary across the thickness direction of the face sheets by the following equation [80,81]:

$$\Phi(x, y, z) = \frac{2z_{1,3}V_0}{h_{1,3}} - \cos\left(\frac{\pi z_{1,3}}{h_{1,3}}\right)\phi(x, y) \tag{13}$$

where V_0 is the externally applied voltage and ϕ is the electric potential function. Also [82]:

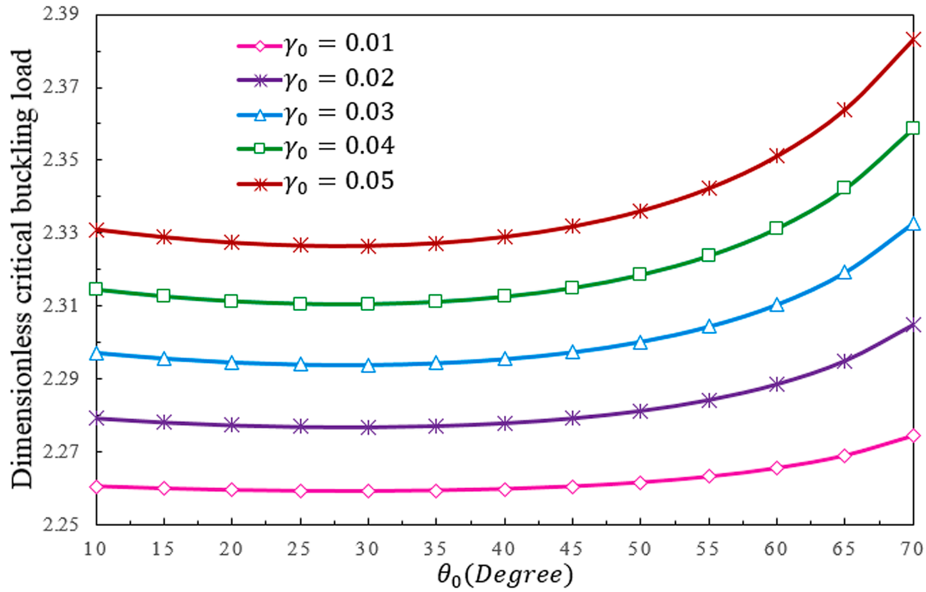

Fig. 5. Geometrical parameters of honeycomb cells effect on the results (Bi-axial).

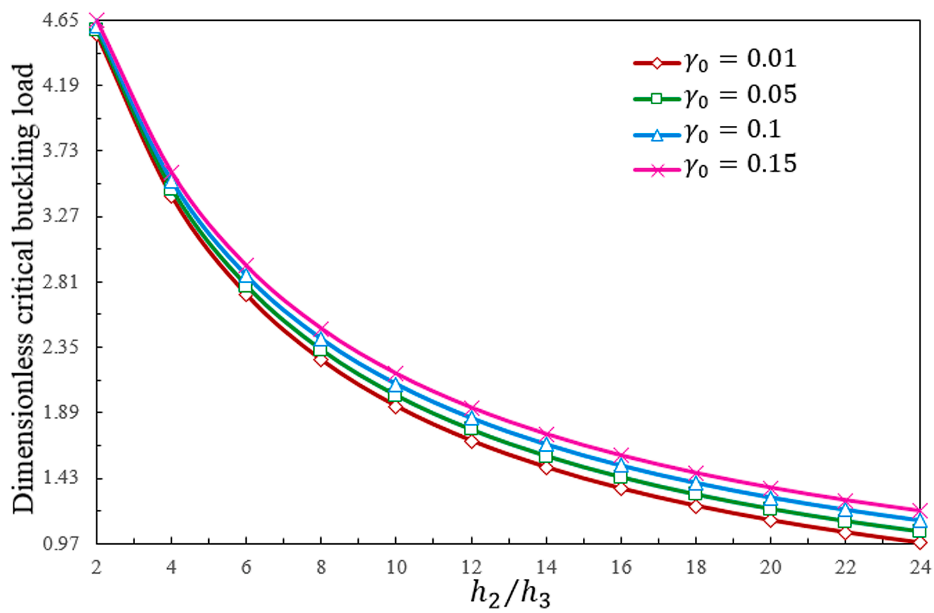

Fig. 6. Effect of the micro plate's thicknesses on the dimensionless critical buckling load (Bi-axial).

$$z_1 = z - \left(\frac{h_2 + h_1}{2}\right), z_3 = z + \left(\frac{h_2 + h_3}{2}\right) \tag{14}$$

Accordingly, the electric field components are determined as [83]:

$$\{ E_x, \quad E_y \} = \left\{ \frac{\partial \phi(x, y)}{\partial x}, \quad \frac{\partial \phi(x, y)}{\partial y} \right\} \cos\left(\frac{\pi z_{1,3}}{h_{1,3}}\right), \tag{15}$$

$$E_z = -\frac{2V_0}{h_{1,3}} - \frac{\pi}{h_{1,3}} \sin\left(\frac{\pi z_{1,3}}{h_{1,3}}\right) \phi(x, y)$$

On the other hand, the electric displacements can be stated in the following matrix form [34]:

$$\begin{Bmatrix} D_x \\ D_y \\ D_z \end{Bmatrix} = \begin{bmatrix} 0 & 0 & 0 & e_{15} & 0 \\ 0 & 0 & e_{24} & 0 & 0 \\ e_{31} & e_{32} & 0 & 0 & 0 \end{bmatrix}^{top,bottom} \begin{Bmatrix} \varepsilon_{xx} \\ \varepsilon_{yy} \\ \gamma_{yz} \\ \gamma_{xz} \\ \gamma_{xy} \end{Bmatrix} + \begin{bmatrix} d_{11} & 0 & 0 \\ 0 & d_{22} & 0 \\ 0 & 0 & d_{33} \end{bmatrix}^{top,bottom} \begin{Bmatrix} E_x \\ E_y \\ E_z \end{Bmatrix} \tag{16}$$

Here D is the electric displacements vector, and d_{ii} represent the dielectric permeability coefficients.

2.3. Kinematic formulations

Based on the SSDT, the displacement components of an arbitrary point of the structure can be described as [63]:

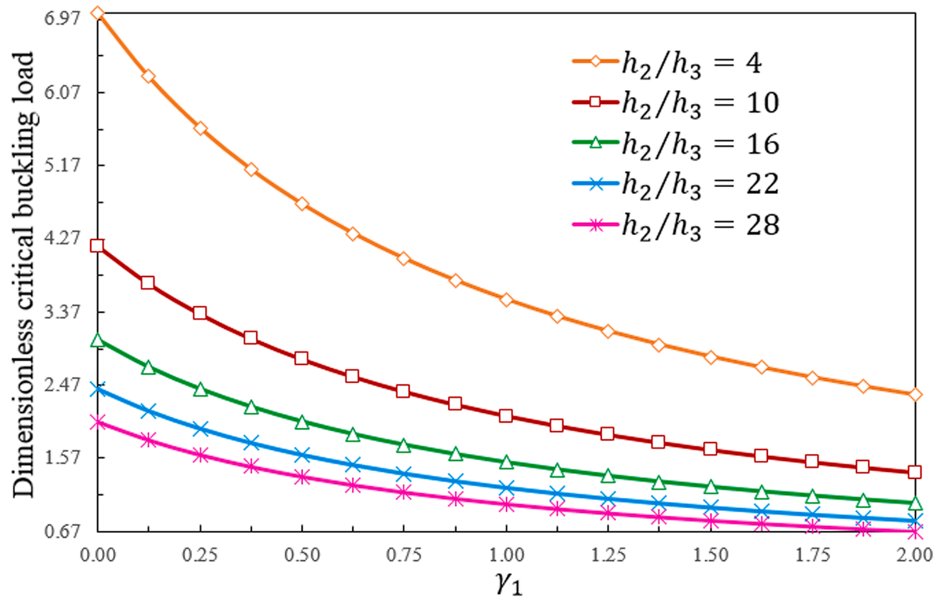

Fig. 7. Magnitude load and thicknesses ratio influence on the results (Uni-axial).

Table 3
Effect of small scale parameter and internal aspect ratio of cells on the dimensionless critical buckling load for different side to thickness ratio in both uni- and bi-axial cases.

		ϕ_0					
a/H	h_2/l_m	Uni-axial buckling load			Bi-axial buckling load		
		0.5	1	2	0.5	1	2
5	1	8.0329	7.9546	7.8966	4.0165	3.9773	3.9483
	2	2.8449	2.7797	2.7246	1.4224	1.3898	1.3623
	3	1.6361	1.5620	1.4916	0.8180	0.7810	0.7458
	4	1.1866	1.1099	1.0304	0.5933	0.5549	0.5152
	5	0.9696	0.8953	0.8138	0.4848	0.4477	0.4069
	6	0.8430	0.7733	0.6937	0.4215	0.3867	0.3469
	7	0.7583	0.6939	0.6182	0.3792	0.3470	0.3091
	8	0.6963	0.6369	0.5658	0.3482	0.3184	0.2829
	9	0.6479	0.5930	0.5267	0.3240	0.2965	0.2634
	10	0.6086	0.5577	0.4959	0.3043	0.2788	0.2479
10	1	8.9154	8.8348	8.7763	4.4577	4.4174	4.3882
	2	3.7070	3.6546	3.6133	1.8535	1.8273	1.8066
	3	2.3497	2.2935	2.2416	1.1748	1.1467	1.1208
	4	1.7641	1.7059	1.6453	0.8820	0.8529	0.8227
	5	1.4441	1.3884	1.3257	0.7221	0.6942	0.6628
	6	1.2405	1.1892	1.1289	0.6202	0.5946	0.5645
	7	1.0973	1.0507	0.9949	0.5487	0.5253	0.4974
	8	0.9899	0.9474	0.8965	0.4950	0.4737	0.4483
	9	0.9056	0.8667	0.8204	0.4528	0.4334	0.4102
	10	0.8373	0.8014	0.7593	0.4187	0.4007	0.3796

$$\widetilde{u}(x,y,z) = u_0(x,y) - z\frac{\partial w_0(x,y)}{\partial x} + \frac{H}{\pi}\sin\left(\frac{\pi z}{H}\right)\lambda_1(x,y), \tag{17}$$

$$\widetilde{v}(x,y,z) = v_0(x,y) - z\frac{\partial w_0(x,y)}{\partial y} + \frac{H}{\pi}\sin\left(\frac{\pi z}{H}\right)\lambda_2(x,y),$$

$$\widetilde{w}(x,y,z) = w_0(x,y)$$

in which the displacements in x, y and z directions are shown by $\widetilde{u}$, $\widetilde{v}$, and $\widetilde{w}$, respectively and the subscript 0 denotes the mid-plane in the mentioned directions. Moreover, λ_1 and λ_2 denote the rotation of the mid-plane about y and x-axes, respectively. According to the Von-Karman's assumptions, the strains are related to the displacement components through the below relations [84]:

$$\varepsilon_{xx} = \frac{\partial}{\partial x}u_0(x,y) - z\left(\frac{\partial^2}{\partial x^2}w_0(x,y)\right) + \frac{H}{\pi}\sin\left(\frac{\pi z}{H}\right)\left(\frac{\partial}{\partial x}\lambda_1(x,y)\right), \tag{18}$$

$$\varepsilon_{yy} = \frac{\partial}{\partial y}v_0(x,y) - z\left(\frac{\partial^2}{\partial y^2}w_0(x,y)\right) + \frac{H}{\pi}\sin\left(\frac{\pi z}{H}\right)\left(\frac{\partial}{\partial y}\lambda_2(x,y)\right),$$

$$\varepsilon_{yz} = \frac{1}{2}\cos\left(\frac{\pi z}{H}\right)\lambda_2(x,y),$$

$$\varepsilon_{xz} = \frac{1}{2}\cos\left(\frac{\pi z}{H}\right)\lambda_1(x,y),$$

$$\varepsilon_{xy} = \frac{1}{2}\frac{\partial}{\partial x}v_0(x,y) - z\left(\frac{\partial^2}{\partial x\partial y}w_0(x,y)\right) + \frac{1}{2}\frac{H}{\pi}\sin\left(\frac{\pi z}{H}\right)\left(\frac{\partial}{\partial x}\lambda_2(x,y)\right) + \frac{1}{2}\frac{\partial}{\partial y}u_0(x,y) + \frac{1}{2}\frac{H}{\pi}\sin\left(\frac{\pi z}{H}\right)\left(\frac{\partial}{\partial y}\lambda_1(x,y)\right)$$

3. Governing equations

The virtual displacement principle was employed to derive the governing equations based on the MCST as well as SSDT [85]:

$$\delta(U - \Sigma) = 0 \tag{19}$$

In Eq. (19) U and Σ are the strain energy and work of external loads, respectively. Therefore, the strain energy and its variations should be firstly considered.

Based on the MCST, the variation of the strain energy in each layer of the microplate can be stated as [29,86]:

$$\delta U = \int_V \left[\begin{array}{c} \left(\begin{array}{c} \sigma_{xx}\delta\varepsilon_{xx} + \sigma_{yy}\delta\varepsilon_{yy} + \sigma_{xy}\delta\gamma_{xy} + \sigma_{yz}\delta\gamma_{yz} + \sigma_{xz}\delta\gamma_{xz} \\ + m_{xx}\delta\chi_{xx} + m_{yy}\delta\chi_{yy} + 2m_{xy}\delta\chi_{xy} + 2m_{yz}\delta\chi_{yz} + 2m_{xz}\delta\chi_{xz} \\ - D_x\delta E_x - D_y\delta E_y - D_z\delta E_z \end{array}\right)^{top} \\ + \left(\begin{array}{c} \sigma_{xx}\delta\varepsilon_{xx} + \sigma_{yy}\delta\varepsilon_{yy} + \sigma_{xy}\delta\gamma_{xy} + \sigma_{yz}\delta\gamma_{yz} + \sigma_{xz}\delta\gamma_{xz} \\ + m_{xx}\delta\chi_{xx} + m_{yy}\delta\chi_{yy} + 2m_{xy}\delta\chi_{xy} + 2m_{yz}\delta\chi_{yz} + 2m_{xz}\delta\chi_{xz} \end{array}\right)^{core} \\ + \left(\begin{array}{c} \sigma_{xx}\delta\varepsilon_{xx} + \sigma_{yy}\delta\varepsilon_{yy} + \sigma_{xy}\delta\gamma_{xy} + \sigma_{yz}\delta\gamma_{yz} + \sigma_{xz}\delta\gamma_{xz} \\ + m_{xx}\delta\chi_{xx} + m_{yy}\delta\chi_{yy} + 2m_{xy}\delta\chi_{xy} + 2m_{yz}\delta\chi_{yz} + 2m_{xz}\delta\chi_{xz} \\ - D_x\delta E_x - D_y\delta E_y - D_z\delta E_z \end{array}\right)^{bottom} \end{array}\right] dV \tag{20}$$

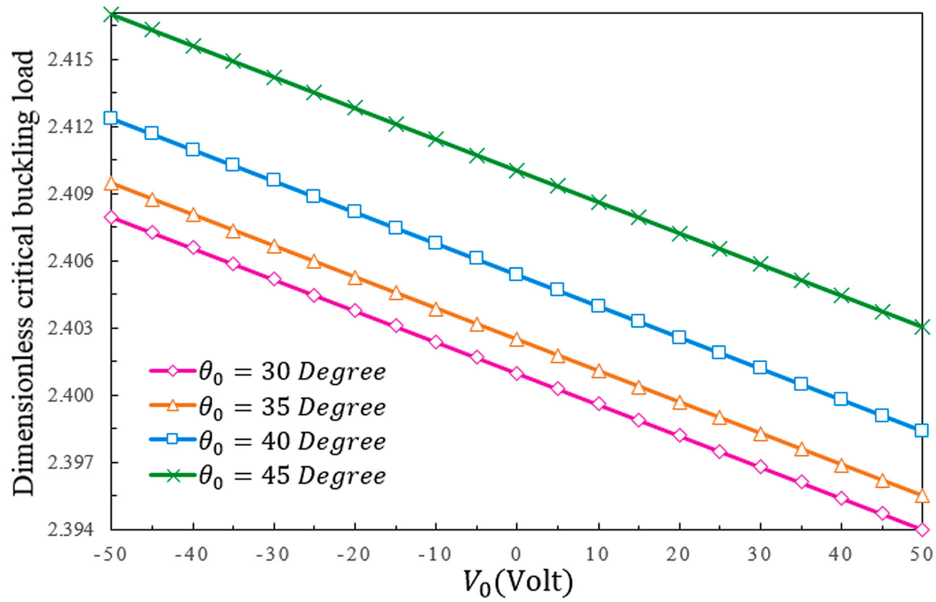

Fig. 8. Effect of electric potential on dimensionless critical buckling load of the microplate (Bi-axial).

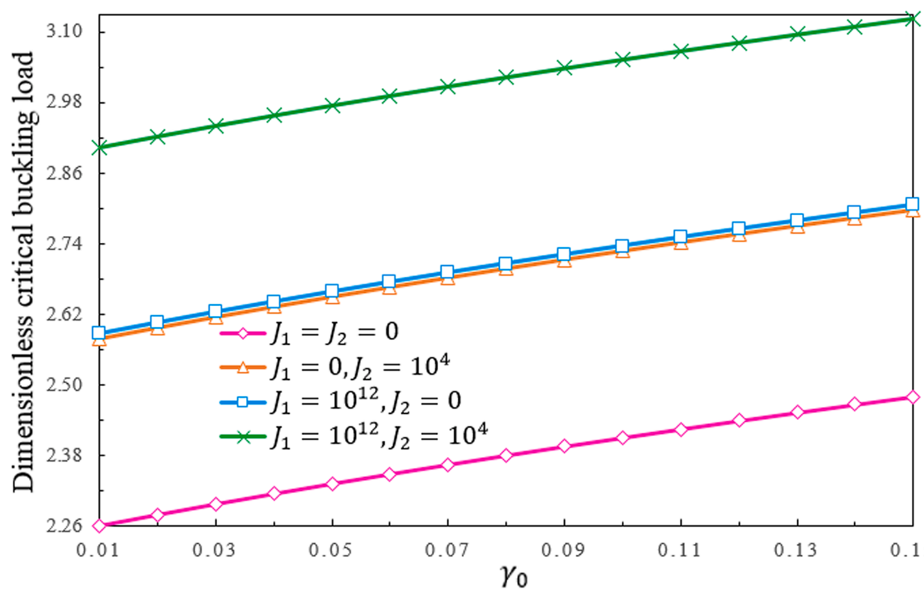

Fig. 9. Comparing the effect of different types of foundation on the results (Bi-axial).

where $m_{ij}^{(s)}$ are the higher-order stress expressed as [78]:

$$m_{ij}^{(s)} = 2\mu l_m^2 \chi_{ij}^{(s)} \tag{21}$$

In the above relation, l_m is the material length-scale parameter, which is suggested by MCST to predict the results in micro dimension, and symmetric rotation gradients $\chi_{ij}^{(s)}$ are defined as follows:

$$\chi_{ij}^{(s)} = \frac{1}{2}\left(\Theta_{i,j} + \Theta_{j,i}\right); \Theta_i = \frac{1}{2}(curl(U))_{,i} \tag{22}$$

in which U denotes the displacements vector, and the infinitesimal rotation vector is presented by Θ. It should be noted that based on MCST, the rotation is applied as a variable to describe curvature. Also, it is known that the MCST is a special format of the MSGT.

Moreover, the Lame's parameter can be presented by μ:

$$\mu = \frac{E}{2(1+\nu)} \tag{23}$$

By inserting the displacement components of Eq. (17) in the above equations, below relations are obtained for deviatoric stretch gradient tensor arrays:

$$\chi_{xx}^{(s)} = \frac{\partial^2 w_0}{\partial x \partial y} - \frac{1}{2}\cos\left(\frac{\pi z}{H}\right)\frac{\partial \lambda_2}{\partial x}, \tag{24}$$

$$\chi_{yy}^{(s)} = -\frac{\partial^2 w_0}{\partial x \partial y} + \frac{1}{2}\cos\left(\frac{\pi z}{H}\right)\frac{\partial \lambda_1}{\partial y},$$

$$\chi_{zz}^{(s)} = \frac{1}{2}\cos\left(\frac{\pi z}{H}\right)\left(\frac{\partial \lambda_2}{\partial x} - \frac{\partial \lambda_1}{\partial y}\right),$$

$$\chi_{xy}^{(s)} = \frac{1}{2}\left(\frac{\partial^2 w_0}{\partial y^2} - \frac{\partial^2 w_0}{\partial x^2}\right) + \frac{1}{4}\cos\left(\frac{\pi z}{H}\right)\left(\frac{\partial \lambda_1}{\partial x} - \frac{\partial \lambda_2}{\partial y}\right),$$

$$\chi_{yz}^{(s)} = \frac{1}{4}\left(\frac{\partial^2 v_0}{\partial x \partial y} - \frac{\partial^2 u_0}{\partial y^2}\right) + \frac{1}{4}\frac{H}{\pi}\sin\left(\frac{\pi z}{H}\right)\left(\frac{\partial^2 \lambda_2}{\partial x \partial y} - \frac{\partial^2 \lambda_1}{\partial y^2}\right) - \frac{1}{4}\frac{\pi}{H}\sin\left(\frac{\pi z}{H}\right)\lambda_1,$$

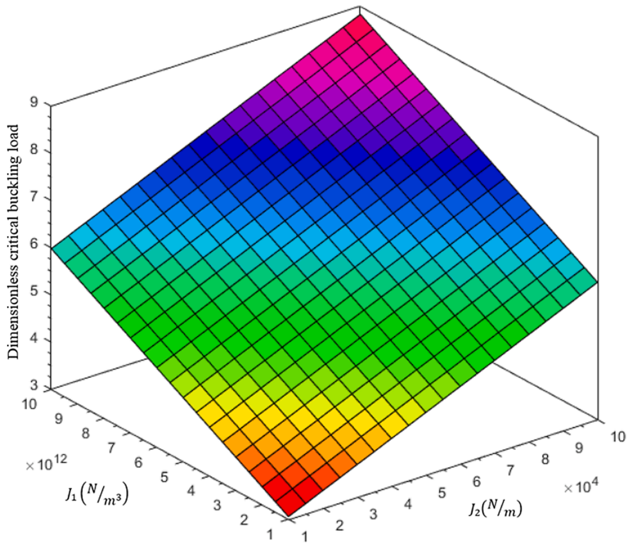

Fig. 10. Effect of both springs and shear layer parameters on the dimensionless critical buckling load of the microplate (Bi-axial).

$$\chi_{xz}^{(s)}=\frac{1}{4}\left(\frac{\partial^2 v_0}{\partial x^2}-\frac{\partial^2 u_0}{\partial x\partial y}\right)+\frac{1}{4}\frac{H}{\pi}\sin\left(\frac{\pi z}{H}\right)\left(\frac{\partial^2\lambda_2}{\partial x^2}-\frac{\partial^2\lambda_1}{\partial x\partial y}\right)+\frac{1}{4}\frac{\pi}{H}\sin\left(\frac{\pi z}{H}\right)\lambda_2$$

Consequently, the expression for variations of the strain energy can be written as:

$$\overline{D}_z=\int_{h_{1,3}}\frac{\pi}{h_{1,3}}\sin\left(\frac{\pi z_{1,3}}{h_{1,3}}\right)D_z\,\mathrm{d}z$$

As stated before, the structure rests on an elastic foundation simulated by the Pasternak model. This foundation can stand both normal and shear forces and includes springs and shear layer [87]. Moreover, voltage is applied to the top and bottom piezoelectric face sheets. To obtain the variations of the work done by the external loads [88]:

$$\delta\Sigma=\int_A\left[-J_1 w_0+J_2\left(\frac{\partial^2 w_0}{\partial x^2}+\frac{\partial^2 w_0}{\partial y^2}\right)-N_{x0}\frac{\partial^2 w_0}{\partial x^2}-N_{y0}\frac{\partial^2 w_0}{\partial y^2}\right]\delta w_0\,\mathrm{d}A \tag{27}$$

where J_1 and J_2 denote the springs and shear layer parameters, respectively.

Also, N_{x0} and N_{y0} are the applied loads in the x and y directions, respectively indicating the mechanical loads a follow:

$$N_{x0}=\gamma_1 N_x+N_x^E\,N_{y0}=\gamma_2 N_y+N_y^E \tag{28}$$

in which γ_1 and γ_2 are the load magnitude in x and y directions, respectively. For the bi-axial buckling case, both of them are non-zero. However, for the uni-axial case, one of them depends on the load direction and will be neglected (set equal to zero). Also, N_x^E and N_y^E are the applied electric potentials in x and y directions, respectively.

By replacing the obtained expressions for variations of the strain energy and work of external loads in virtual displacement relation, the governing equations can be derived in terms of displacement components:

$$\delta U=\int_A\left[\begin{array}{c}-\left(\frac{\partial N_{xx}}{\partial x}+\frac{\partial N_{xy}}{\partial y}\frac{1}{2}\frac{\partial^2 Y_{yz}^1}{\partial y^2}+\frac{1}{2}\frac{\partial^2 Y_{xz}^1}{\partial x\partial y}\right)\delta u_0-\left(\frac{\partial N_{yy}}{\partial y}+\frac{\partial N_{xy}}{\partial x}-\frac{1}{2}\frac{\partial^2 Y_{xz}^1}{\partial x^2}-\frac{1}{2}\frac{\partial^2 Y_{yz}^1}{\partial x\partial y}\right)\delta v_0\\ -\left(\frac{\partial^2 M_{xx}}{\partial x^2}+\frac{\partial^2 M_{yy}}{\partial y^2}+2\frac{\partial^2 M_{xy}}{\partial x\partial y}-\frac{\partial^2 Y_{xy}^1}{\partial y^2}+\frac{\partial^2 Y_{xy}^1}{\partial x^2}+\frac{\partial^2 Y_{yy}^1}{\partial x\partial y}-\frac{\partial^2 Y_{xx}^1}{\partial x\partial y}\right)\delta w_0\\ +\left(-\frac{\partial P_{xx}}{\partial x}-\frac{\partial P_{xy}}{\partial y}+R_{xz}-\frac{1}{2}\frac{\partial^2 Y_{yz}^2}{\partial y^2}-\frac{1}{2}\frac{\partial^2 Y_{xz}^2}{\partial x\partial y}+\frac{1}{2}Y_{yz}^4-\frac{1}{2}\frac{\partial Y_{xy}^3}{\partial x}-\frac{1}{2}\frac{\partial Y_{yy}^3}{\partial y}+\frac{1}{2}\frac{\partial Y_{zz}^3}{\partial y}\right)\delta\lambda_1\\ +\left(-\frac{\partial P_{yy}}{\partial y}-\frac{\partial P_{xy}}{\partial x}+R_{yz}+\frac{1}{2}\frac{\partial^2 Y_{xz}^2}{\partial x^2}-\frac{1}{2}Y_{xz}^4+\frac{1}{2}\frac{\partial^2 Y_{yz}^2}{\partial x\partial y}-\frac{1}{2}\frac{\partial Y_{zz}^3}{\partial x}+\frac{1}{2}\frac{\partial Y_{xy}^3}{\partial y}+\frac{1}{2}\frac{\partial Y_{xx}^3}{\partial x}\right)\delta\lambda_2\\ +\left(\frac{\partial\overline{D}_x}{\partial x}+\frac{\partial\overline{D}_y}{\partial y}+\overline{D}_z\right)\delta\phi\end{array}\right]\mathrm{d}A \tag{25}$$

in which the classical and higher-order stress resultants used in the above equation are expressed as:

$$\left[N_{ij},\quad M_{ij},\quad P_{ij},\quad R_{ij}\right]=\int_{-H/2}^{H/2}\sigma_{ij}\left[1,\quad z,\quad \frac{H}{\pi}\sin\left(\frac{\pi z}{H}\right),\quad \cos\left(\frac{\pi z}{H}\right)\right]\mathrm{d}z, \tag{26}$$

$$\left[Y_{ij}^1,\ Y_{ij}^2,\ Y_{ij}^3,\ Y_{ij}^4\right]=\int_{-H/2}^{H/2}m_{ij}\left[1,\ \frac{H}{\pi}\sin\left(\frac{\pi z}{H}\right),\ \cos\left(\frac{\pi z}{H}\right),\ -\frac{\pi}{H}\sin\left(\frac{\pi z}{H}\right)\right]\mathrm{d}z,$$

$$\left[\overline{D}_x,\quad \overline{D}_y\right]=\int_{h_{1,3}}\cos\left(\frac{\pi z_{1,3}}{h_{1,3}}\right)\left[D_x,\quad D_y\right]\mathrm{d}z,$$

δu_0 :

$$\begin{gathered}\eta_{11}\frac{\partial}{\partial x}\phi-\eta_6\frac{\partial^3}{\partial x^3}w_0+\eta_7\frac{\partial^2}{\partial x^2}\lambda_1+\eta_8\frac{\partial^2}{\partial y\partial x}v_0-\eta_9\frac{\partial^3}{\partial y^2\partial x}w_0+\eta_{10}\frac{\partial^2}{\partial y\partial x}\lambda_2-\eta_{13}\frac{\partial^2}{\partial y\partial x}v_0\\ +2\eta_{14}\frac{\partial^3}{\partial y^2\partial x}w_0-\eta_{15}\frac{\partial^2}{\partial y\partial x}\lambda_2-\eta_{13}\frac{\partial^2}{\partial y^2}u_0-\eta_{15}\frac{\partial^2}{\partial y^2}\lambda_1+\eta_5\frac{\partial^2}{\partial x^2}u_0+\frac{1}{8}\eta_2\frac{\partial^4}{\partial y^2\partial x^2}\lambda_1\\ -\frac{1}{8}\eta_3\frac{\partial^2}{\partial y^2}\lambda_1-\frac{1}{8}\eta_1\frac{\partial^4}{\partial y^3\partial x}v_0-\frac{1}{8}\eta_2\frac{\partial^4}{\partial y^3\partial x}\lambda_2+\frac{1}{8}\eta_1\frac{\partial^4}{\partial y^4}u_0+\frac{1}{8}\eta_2\frac{\partial^4}{\partial y^4}\lambda_1+\frac{1}{8}\eta_3\frac{\partial^2}{\partial y\partial x}\lambda_2\\ -\frac{1}{8}\eta_1\frac{\partial^4}{\partial y\partial x^3}v_0-\frac{1}{8}\eta_2\frac{\partial^4}{\partial y\partial x^3}\lambda_2+\frac{1}{8}\eta_1\frac{\partial^4}{\partial y^2\partial x^2}u_0=0\end{gathered} \tag{29}$$

δv_0 :

$$\begin{aligned}
&2\eta_{14}\frac{\partial^3}{\partial y\partial x^2}w_0-\eta_{15}\frac{\partial^2}{\partial x^2}\lambda_2-\eta_{13}\frac{\partial^2}{\partial y\partial x}u_0+\eta_{15}\frac{\partial^2}{\partial y\partial x}\lambda_1+\eta_{17}\frac{\partial^3}{\partial y^3}w_0+\eta_{18}\frac{\partial^2}{\partial y^2}\lambda_2-\eta_{13}\frac{\partial^2}{\partial x^2}v_0\\
&+\eta_9\frac{\partial^3}{\partial y\partial x^2}w_0-\eta_{10}\frac{\partial^2}{\partial y\partial x}\lambda_1-\eta_{16}\frac{\partial^2}{\partial y^2}v_0-\eta_8\frac{\partial^2}{\partial y\partial x}u_0-\frac{1}{8}\eta_1\frac{\partial^4}{\partial y\partial x^3}u_0+\frac{1}{8}\eta_2\frac{\partial^4}{\partial y\partial x^3}\lambda_1\\
&+\frac{1}{8}\eta_3\frac{\partial^2}{\partial y\partial x}\lambda_1+\frac{1}{8}\eta_1\frac{\partial^4}{\partial y^2\partial x^2}v_0+\frac{1}{8}\eta_2\frac{\partial^4}{\partial y^2\partial x^2}\lambda_2-\frac{1}{8}\eta_1\frac{\partial^4}{\partial y^3\partial x}u_0-\frac{1}{8}\eta_2\frac{\partial^4}{\partial y^3\partial x}\lambda_1-\frac{1}{8}\eta_3\frac{\partial^2}{\partial x^2}\lambda_2\\
&+\frac{1}{8}\eta_1\frac{\partial^4}{\partial x^4}v_0+\frac{1}{8}\eta_2\frac{\partial^4}{\partial x^4}\lambda_2-\eta_{19}\frac{\partial}{\partial y}\phi=0
\end{aligned}\tag{30}$$

δw_0 :

$$\begin{aligned}
&\frac{1}{4}\eta_{21}\frac{\partial^3}{\partial x^3}\lambda_1-\frac{1}{2}\eta_1\frac{\partial^4}{\partial x^4}w_0+\frac{1}{4}\eta_{21}\frac{\partial^3}{\partial y\partial x^2}\lambda_2-2\eta_1\frac{\partial^4}{\partial y^2\partial x^2}w_0-\frac{1}{4}\eta_{21}\frac{\partial^3}{\partial y^3}\lambda_2+\frac{1}{2}\eta_1\frac{\partial^4}{\partial y^4}w_0\\
&+\frac{3}{4}\eta_{21}\frac{\partial^3}{\partial y^2\partial x}\lambda_1+2\eta_{25}\frac{\partial^3}{\partial y\partial x^2}v_0-4\eta_{26}\frac{\partial^4}{\partial y^2\partial x^2}w_0+2\eta_{27}\frac{\partial^3}{\partial y\partial x^2}\lambda_2+2\eta_{25}\frac{\partial^3}{\partial y^2\partial x}u_0\\
&+2\eta_{27}\frac{\partial^3}{\partial y^2\partial x}\lambda_1-\eta_{59}\frac{\partial^3}{\partial y^2\partial x}u_0+\eta_{60}\frac{\partial^4}{\partial y^2\partial x^2}w_0-\eta_{61}\frac{\partial^3}{\partial y^2\partial x}\lambda_1-\eta_{22}\frac{\partial^3}{\partial y^3}v_0+\eta_{23}\frac{\partial^4}{\partial y^4}w_0\\
&-\eta_{24}\frac{\partial^3}{\partial y^3}\lambda_2-\eta_{20}\frac{\partial^2}{\partial y^2}\phi+F_f+\eta_{60}\frac{\partial^4}{\partial y^2\partial x^2}w_0-\eta_{28}\frac{\partial^3}{\partial x^3}u_0+\eta_{29}\frac{\partial^4}{\partial x^4}w_0-\eta_{30}\frac{\partial^3}{\partial x^3}\lambda_1\\
&-\eta_{59}\frac{\partial^3}{\partial y\partial x^2}v_0-\eta_{61}\frac{\partial^3}{\partial y\partial x^2}\lambda_2-\eta_{12}\frac{\partial^2}{\partial x^2}\phi=0
\end{aligned}\tag{31}$$

$\delta\lambda_1$:

$$\begin{aligned}
&\frac{1}{8}\eta_{43}\frac{\partial^2}{\partial y\partial x}v_0+\frac{1}{8}\eta_{44}\frac{\partial^2}{\partial y\partial x}\lambda_2-\frac{1}{8}\eta_{43}\frac{\partial^2}{\partial y^2}u_0-\frac{1}{8}\eta_{44}\frac{\partial^2}{\partial y^2}\lambda_1+\frac{1}{8}\eta_{41}\frac{\partial^4}{\partial y^2\partial x^2}\lambda_1+\frac{1}{8}\eta_{42}\frac{\partial^2}{\partial y\partial x}\lambda_2\\
&-\frac{1}{8}\eta_{40}\frac{\partial^4}{\partial y\partial x^3}v_0-\frac{1}{8}\eta_{41}\frac{\partial^4}{\partial y\partial x^3}\lambda_2+\frac{1}{8}\eta_{40}\frac{\partial^4}{\partial y^2\partial x^2}u_0-\eta_{37}\frac{\partial^3}{\partial y^2\partial x}w_0+\eta_{38}\frac{\partial^2}{\partial y\partial x}\lambda_2-\eta_{34}\frac{\partial^3}{\partial x^3}w_0\\
&+\eta_{35}\frac{\partial^2}{\partial x^2}\lambda_1+\eta_{36}\frac{\partial^2}{\partial y\partial x}v_0+\eta_{33}\frac{\partial^2}{\partial x^2}u_0+\eta_{39}\frac{\partial^4}{\partial y\partial x^3}\lambda_2+\eta_{39}\frac{\partial^4}{\partial x^4}\lambda_1+\frac{1}{8}\eta_{45}\lambda_1-\eta_{39}\frac{\partial}{\partial x}\phi-\eta_{31}\lambda_1\\
&+\eta_{32}\frac{\partial}{\partial x}\phi-\frac{1}{8}\eta_{46}\frac{\partial^2}{\partial x^2}\lambda_1+\frac{1}{4}\eta_{21}\frac{\partial^3}{\partial x^3}w_0-\frac{1}{8}\eta_{46}\frac{\partial^2}{\partial y\partial x}\lambda_2+\frac{1}{4}\eta_{46}\frac{\partial^2}{\partial y^2}\psi_1-\frac{1}{4}\eta_{21}\frac{\partial^3}{\partial y^2\partial x}w_0\\
&+2\eta_{27}\frac{\partial^3}{\partial y^2\partial x}w_0-\eta_{47}\frac{\partial^2}{\partial y\partial x}\lambda_2-\eta_{15}\frac{\partial^2}{\partial y^2}u_0-\eta_{47}\frac{\partial^2}{\partial y^2}\lambda_1-\eta_{15}\frac{\partial^2}{\partial y\partial x}v_0-\frac{1}{4}\eta_{46}\frac{\partial^2}{\partial y^2}\lambda_1\\
&+\frac{1}{2}\eta_{21}\frac{\partial^3}{\partial y^2\partial x}w_0+\eta_{39}\frac{\partial^4}{\partial y^2\partial x^2}\lambda_1+\eta_{39}\frac{\partial^4}{\partial y^3\partial x}\lambda_2-\frac{1}{8}\eta_{42}\frac{\partial^2}{\partial y^2}\lambda_1-\frac{1}{8}\eta_{40}\frac{\partial^4}{\partial y^3\partial x}v_0\\
&-\frac{1}{8}\eta_{41}\frac{\partial^4}{\partial y^3\partial x}\lambda_2+\frac{1}{8}\eta_{40}\frac{\partial^4}{\partial y^4}u_0+\frac{1}{8}\eta_{41}\frac{\partial^4}{\partial y^4}\lambda_1=0
\end{aligned}\tag{32}$$

$\delta\lambda_2$:

$$\begin{aligned}
&\frac{1}{8}\eta_{45}\lambda_2-\eta_{56}\frac{\partial}{\partial y}\phi+\eta_{54}\lambda_2+2\eta_{27}\frac{\partial^3}{\partial y\partial x^2}w_0-\eta_{47}\frac{\partial^2}{\partial x^2}\lambda_2-\eta_{15}\frac{\partial^2}{\partial y\partial x}u_0-\eta_{47}\frac{\partial^2}{\partial y\partial x}\lambda_1\\
&+\frac{1}{8}\eta_{41}\frac{\partial^4}{\partial y^3\partial x}\lambda_1-\eta_{15}\frac{\partial^2}{\partial x^2}v_0+\frac{1}{8}\eta_{42}\frac{\partial^2}{\partial y\partial x}\lambda_1-\frac{1}{8}\eta_{40}\frac{\partial^4}{\partial y^2\partial x^2}v_0-\frac{1}{8}\eta_{41}\frac{\partial^4}{\partial y^2\partial x^2}\lambda_2\\
&-\frac{1}{8}\eta_{40}\frac{\partial^4}{\partial y^3\partial x}u_0+\eta_{58}\frac{\partial^2}{\partial y^2}\lambda_2-\eta_{37}\frac{\partial^3}{\partial y\partial x^2}w_0+\eta_{38}\frac{\partial^2}{\partial y\partial x}\lambda_1+\eta_{57}\frac{\partial^2}{\partial y^2}v_0-\eta_{56}\frac{\partial^3}{\partial y^3}w_0\\
&+\eta_{36}\frac{\partial^2}{\partial y\partial x}u_0+\eta_{58}\frac{\partial}{\partial y}\phi-\frac{1}{8}\eta_{44}\frac{\partial^2}{\partial y\partial x}\lambda_1-\frac{1}{2}\eta_{21}\frac{\partial^3}{\partial y\partial x^2}w_0+\frac{1}{4}\eta_{46}\frac{\partial^2}{\partial x^2}\lambda_2+\frac{1}{8}\eta_{43}\frac{\partial^2}{\partial x^2}v_0\\
&-\frac{1}{8}\eta_{44}\frac{\partial^2}{\partial x^2}\lambda_2-\frac{1}{8}\eta_{43}\frac{\partial^2}{\partial y\partial x}u_0-\frac{1}{8}\eta_{46}\frac{\partial^2}{\partial y^2}\lambda_2+\frac{1}{4}\eta_{21}\frac{\partial^3}{\partial y^3}w_0-\frac{1}{8}\eta_{46}\frac{\partial^2}{\partial y\partial x}\lambda_1-\eta_{39}\frac{\partial^4}{\partial y^2\partial x^2}\lambda_2\\
&+\eta_{39}\frac{\partial^4}{\partial y\partial x^3}\lambda_1-\eta_{39}\frac{\partial^4}{\partial y^3\partial x}\lambda_1-\eta_{39}\frac{\partial^4}{\partial y^4}\lambda_2-\frac{1}{4}\eta_{21}\frac{\partial^3}{\partial y\partial x^2}w_0+\frac{1}{4}\eta_{46}\frac{\partial^2}{\partial x^2}\lambda_2-\frac{1}{8}\eta_{42}\frac{\partial^2}{\partial x^2}\lambda_2\\
&-\frac{1}{8}\eta_{40}\frac{\partial^4}{\partial x^4}v_0+\frac{1}{8}\eta_{41}\frac{\partial^4}{\partial x^4}\lambda_2+\frac{1}{8}\eta_{40}\frac{\partial^4}{\partial y\partial x^3}u_0+\frac{1}{8}\eta_{41}\frac{\partial^4}{\partial y\partial x^3}\lambda_1=0
\end{aligned}\tag{33}$$

$\delta\phi$:

$$\eta_{51}\frac{\partial}{\partial x}\lambda_1+\eta_{48}\frac{\partial^2}{\partial x^2}\phi+\eta_{52}\frac{\partial}{\partial y}\lambda_2+\eta_{50}\frac{\partial^2}{\partial y^2}\phi+\eta_{53}\frac{\partial}{\partial x}u_0-\eta_{54}\frac{\partial^2}{\partial x^2}w_0+\eta_{55}\frac{\partial}{\partial x}\lambda_1+\eta_{56}\frac{\partial}{\partial y}v_0 -\eta_{57}\frac{\partial^2}{\partial y^2}w_0+\eta_{58}\frac{\partial}{\partial y}\lambda_2-\eta_{49}\phi=0 \tag{34}$$

The coefficients used in Eqs. (29)-(34) are defined in Appendix A.

4. Analytical solution approach

There are different solution methods to solve the differential equations system that some of them are analytical and some are numerical. The most well-known and accurate of analytical solution approaches is Navier's method which presents the double series Fourier type functions as the unknown variables for simply supported edges boundary conditions. Other solution approaches such as finite element method, finite difference method, Galerkin, and generalized differential quadrature method are other solution methods that can achieve the results for other types of boundary conditions based on them [89–92]. As stated, based on Navier's solution method, the displacements are considered as functions satisfying the simply supported boundary conditions at the edges of the structure [93]. So, the following functions can be considered for displacement components [94]:

$$\begin{Bmatrix} u_0 \\ v_0 \\ w_0 \\ \lambda_1 \\ \lambda_2 \\ \phi \end{Bmatrix} = \sum_{m=1}^{\infty}\sum_{n=1}^{\infty}\begin{Bmatrix} U\cos(\alpha x)\sin(\beta y) \\ V\sin(\alpha x)\cos(\beta y) \\ W\sin(\alpha x)\sin(\beta y) \\ \Xi_1\cos(\alpha x)\sin(\beta y) \\ \Xi_2\sin(\alpha x)\cos(\beta y) \\ \Phi\sin(\alpha x)\sin(\beta y) \end{Bmatrix} \tag{35}$$

where U, V, W, Ξ_1, Ξ_2, and Φ are amplitudes of displacements and rotations of the microplate. Furthermore, $\alpha = m\pi/a$ and $\beta = n\pi/b$. Substituting the proposed functions in the governing equations of (29)-(34) yields:

$$([K_e] - P_{cr}[K_g])\{X\} = 0 \tag{36}$$

in which $[K_e]$ and $[K_g]$ are the stiffness and geometric stiffness matrix, respectively whose components are introduced in Appendix B. P_{cr} also denotes the critical buckling load. Furthermore, $\{X\}$ is the displacements vector. Solving this eigenvalue problem results in the critical buckling load of the structure. It should be noted that the critical buckling load is achieved by setting $m = n = 1$.

5. Results and discussion

Before presenting and analyzing the results, their reliability should be examined. To validate the results with the known data in the open literature, the results for the simple state were considered as this work was the first study with the mentioned specifications. Table 1 lists the results for a size-dependent FG rectangular microplate considering the size effect based on MCST in absence of an elastic foundation. These results were and compared with those of Hen *et al.* [95]. In this table, the dimensionless critical buckling load is defined as $\frac{N_x a^2}{EH^3}$. The results are obtained for different side to thickness ratios, dimensionless small-scale parameter, and also, for various gradient index of n which shows the distribution of FG materials across the thickness direction. It should be noted in He *et al.* [95] work, the following functions are regarded for grading the properties:

$$E(z) = E_2 + (E_1 - E_2)\left(\frac{1}{2}+\frac{z}{h}\right)^n, \tag{37}$$

$$\rho(z) = \rho_2 + (\rho_1 - \rho_2)\left(\frac{1}{2}+\frac{z}{h}\right)^n,$$

$$\nu(z) = \nu_2 + (\nu_1 - \nu_2)\left(\frac{1}{2}+\frac{z}{h}\right)^n$$

An excellent agreement can be observed between the present results and those of He *et al.* [95] and a slight difference can be attributed to different descriptions of displacement. He *et al.* [95] used a refined four-variable shear deformation theory while the present work exploited a higher-order one with a sinusoidal function. As the second step to validate the results, the buckling load ratios (i.e. ratio of the results for microplate to those of macro plate) of a piezoelectric ($BaTiO_3$) square microplate are obtained and compared to those of Jamalpour *et al.* [96] in Table 2. The results are listed for various electric potential V_0 and different non-dimensional length-scale parameter (H/l_m) and plate thicknesses are given in Table 2. As can be seen, the results are in good agreement with each other. Consequently, the reliability of the formulations and solution method is ensured. In the following, the current study results will be illustrated.

Now, the results of the current study will be depicted in both uni-axial and bi-axial buckling cases. It is noteworthy that aluminum was selected for the honeycomb core with $E = 70$ GPa, $\rho = 2702$ kg/m^3, and $\nu = 0.3$ [76]. On the other hand, $BaTiO_3$ was chosen as the piezoelectric facesheets whose electro-mechanical properties are defined as follows [63]:

$c_{11} = c_{22} = 226$ *GPa*,	$c_{12} = 125$ *GPa*,	$c_{44} = c_{55} = 44.2$ *GPa*,	$c_{66} = 50.5$ *GPa*,
$\rho = 5550$ kg/m^3, $d_{33} = 6.35 \times 10^{-9} F/m$.	$e_{31} = e_{32} = -2.2 C/m^2$,	$e_{15} = e_{24} = 5.8 C/m^2$,	$d_{11} = d_{22} = 5.64 \times 10^{-9} F/m$,

For all of the following results except those noted, the small-scale parameter was set 15 μm. Length and width of the microplate were equal and 10 times more than the total thickness of the structure, $h_2/l = 3$, $\theta_0 = 45^\circ$, $\gamma_0 = 0.1$, and $\phi_0 = 1$. In addition, the thicknesses of the face sheets were similar and equal to 3 μm.

The effect of load magnitudes, in both x and y directions, on the dimensionless critical buckling load is depicted in Fig. 2. As stated before, γ_1 and γ_2 are the magnitudes of the in-plane applied load in x and y directions, respectively. According to this figure, as expected, the dimensionless critical buckling load of the microplate is reduced by increasing both of these parameters. Note that setting each of these parameters converts the applied load to the uni-axial case. In fact, by applying both γ_1 and γ_2, the stability of the structure will be declined, thus its critical buckling load will decrease. This also holds for their magnitudes.

Two geometrical factors of honeycomb cells namely, internal aspect ratio and their angle (ϕ_0 and θ_0, respectively) are depicted in Fig. 3. By increasing the internal aspect ratio, the dimensionless critical buckling load reduced; for angle effect, however, it's a bit different. The effect of the cells' angle depends on the internal aspect ratio value. As suggested by Fig. 3, for higher values of the internal aspect ratio, an increase in the cell angle led to an enhancement in dimensionless critical buckling load. For lower values of ϕ_0, it started to grow after a slight decrease. The reason for this phenomenon could be searched in variations in the microstructures' stiffness. By reduction of the stiffness, the critical buckling load also decreased, and vice versa.

The effect of another geometrical specification of honeycomb cells is depicted in Fig. 4. By enhancing γ_0 (dimensionless thickness of honeycomb cells), the stiffness of the structure grew, and accordingly, its critical buckling load increased. Furthermore, Fig. 4 considers the size effect. Based on this figure, the critical buckling load reduced upon enhancing the h_2/l_m ratio. This effect got pronounced for lower values.

In the case of bi-axial buckling, Fig. 5 plots the variations of dimensionless critical buckling load concerning two parameters simultaneously. The first one is the dimensionless thickness of honeycomb while the second one is their angle. This figure confirms the previous findings on the changes in stiffness of the structures and hence, its dimensionless critical buckling load.

Fig. 6 investigates the effect of the thicknesses ratio on the dimensionless critical buckling load. As can be seen, an increase in the core thickness (h_2) incremented the structure softness giving rise to a reduction in dimensionless critical buckling load. This figure is drawn by at constant the total thickness of the microplate. In other words, the decrease in stiffness of the structure implies that the stiffness of the faces is more than the core.

Fig. 7 illustrates the simultaneous effect of thicknesses ratio and the load magnitude. Similar to the previous graphs, an increase in the load magnitude in the uni-axial buckling case, leads the result to reduce.

Table 3 lists three different effects on the dimensionless critical buckling load; the results are presented with their exact values. The first effect is for ϕ_0, the internal aspect ratio of honeycomb cells. An increase in ϕ_0 declined the results due to the structure softening. The second effect is about the core's thickness to the small-scale parameter ratio. It seems that by elevating this ratio, the dimensionless critical buckling load decremented due to a reduction in the stiffness of the structure. Finally, the third effect is related to the side-to-thickness ratio. Although increasing this ratio softened the structure and declined the critical buckling load, the results of this part showed an increasing manner instead of decreasing trend due to using the mentioned relation for de-dimensionalizing the critical buckling load.

Fig. 8 shows the effect of applied electric potential to the piezoelectric face sheets on the dimensionless critical buckling load. It is seen due to decreasing in the stiffness of the microplate in a result of applying voltage, the critical buckling load reduces. It occurs for all plotted cells' angles.

Up to now, the effect of foundation parameters on the results was not considered. This effect is addressed in Figs. 9 and 10. Fig. 9 compares different types of elastic foundations with various parameters. Instance, the foundation is neglected by setting both J_1 and J_2 to zero. Similarly, three other types are investigated. The results revealed that when both springs and shear layer parameters are non-zero, the critical buckling load is higher than the other three types. It should be noted that setting the foundation parameters to zero makes it less rigid and accordingly, the critical buckling load for this case will be less than other types of foundation.

Fig. 10 depicts the simultaneous influence of the springs and shear layer parameters of the elastic foundation (i.e. J_1 and J_2) in a 3D graph. It can be seen that an increment in both J_1 and J_2 enhanced the dimensionless critical buckling load due to an increase in the microplate rigidity.

6. Conclusions

The current work addressed the mechanical buckling behavior of a three-layered microplate made of honeycomb structures and two piezoelectric face sheets bonded to its top and bottom surfaces. The three layers are fully bonded to each other and the microplate is located on an elastic foundation capable of standing both normal and shearing loads. Minghui and Jiuren relations were employed to determine the effective mechanical properties of the honeycomb core. The SSDT was applied as a higher-order theory with trigonometric shear deformation function to describe the displacement components of the microplate. Using MCST, which employs a material length-scale parameter, the micro dimension effects were taken into account. The governing equations were derived based on the virtual displacement principle. Navier's solution method was chosen for a simply supported edges microplate to analytically extract the critical buckling loads. It was found that by incrementing the internal aspect ratio of the honeycomb cells, the critical buckling load declined. Generally, an increase in the cell angle augmented the critical buckling load. Moreover, an enhancement in the dimensionless thickness of the honeycomb cells raised the critical buckling load. Furthermore, by the growth of the dimensionless length-scale parameter (H/l_m) from one to 15, the results tend to reduce about 94 percent, averagely; this reduction is more significant for lower values of this ratio. Applying the electric potential to the piezoelectric face sheets leads the critical buckling load to reduce. The addition of the elastic foundation, regardless of its type, enhanced the critical buckling load of the microplate. The Pasternak foundation resulted in higher critical buckling loads as compared with the Winkler one.

Declaration of Competing Interest

The authors declare that they have no known competing financial interests or personal relationships that could have appeared to influence the work reported in this paper.

Acknowledgement

This research is financially supported by the Ministry of Science and Technology of China (Grant No.2019YFE0112400), and the Department of Science and Technology of Shandong Province (Grant No. 2021CXGC011204). This research is supported by Abu Dhabi's Advanced Technology Research Council via the ASPIRE Award for Research Excellence program, AARE19-98. Authors acknowledge support received by Taif University Researchers Supporting Project number (TURSP-2020/196), Taif University, Taif, Saudi Arabia.

Appendix A

The coefficients used in Eqs. (29)-(34) are defined as:

$$[\eta_1, \quad \eta_2, \quad \eta_3] = \int_{-H/2}^{H/2} 2\mu l_m^2 \left[1, \quad \frac{H}{\pi}\sin\left(\frac{\pi z}{H}\right), \quad -\frac{\pi}{H}\sin\left(\frac{\pi z}{H}\right)\right] \mathrm{d}z,$$

$$[\eta_5, \quad \eta_6, \quad \eta_7] = \int_{-H/2}^{H/2} Q_{11} \left[1, \quad z, \quad \frac{H}{\pi}\sin\left(\frac{\pi z}{H}\right)\right] \mathrm{d}z,$$

$$[\eta_8, \quad \eta_9, \quad \eta_{10}] = \int_{-H/2}^{H/2} Q_{12} \left[1, \quad z, \quad \frac{H}{\pi}\sin\left(\frac{\pi z}{H}\right)\right] \mathrm{d}z,$$

$$[\eta_{11}, \quad \eta_{12}] = \int_{h_{1,3}} \left(\frac{e_{31}\pi}{h_{1,3}}\sin\left(\frac{\pi z_{1,3}}{h_{1,3}}\right)\right)[1, \quad z]\mathrm{d}z,$$

$$[\eta_{13},\quad \eta_{14},\quad \eta_{15}] = \int_{-H/2}^{H/2} Q_{66}\left[1,\quad z,\quad \frac{H}{\pi}\sin\left(\frac{\pi z}{H}\right)\right]\mathrm{d}z,$$

$$[\eta_{16},\quad \eta_{17},\quad \eta_{18}] = \int_{-H/2}^{H/2} Q_{22}\left[1,\quad z,\quad \frac{H}{\pi}\sin\left(\frac{\pi z}{H}\right)\right]\mathrm{d}z,$$

$$[\eta_{19},\quad \eta_{20}] = \int_{h_{1,3}} \left(\frac{e_{32}\pi}{h_{1,3}}\sin\left(\frac{\pi z_{1,3}}{h_{1,3}}\right)\right)[1,\quad z]\mathrm{d}z,$$

$$\eta_{21} = \int_{-H/2}^{H/2} 2\mu l_m^2 \cos\left(\frac{\pi z}{H}\right)\mathrm{d}z,$$

$$[\eta_{59},\quad \eta_{60},\quad \eta_{61}] = \int_{-H/2}^{H/2} Q_{12}\left[z,\quad z^2,\quad z\frac{H}{\pi}\sin\left(\frac{\pi z}{H}\right)\right]\mathrm{d}z,$$

$$[\eta_{22},\quad \eta_{23},\quad \eta_{24}] = \int_{-H/2}^{H/2} Q_{22}\left[z,\quad z^2,\quad z\frac{H}{\pi}\sin\left(\frac{\pi z}{H}\right)\right]\mathrm{d}z,$$

$$[\eta_{25},\quad \eta_{26},\quad \eta_{27}] = \int_{-H/2}^{H/2} Q_{66}\left[z,\quad z^2,\quad z\frac{H}{\pi}\sin\left(\frac{\pi z}{H}\right)\right]\mathrm{d}z,$$

$$[\eta_{28},\quad \eta_{29},\quad \eta_{30}] = \int_{-H/2}^{H/2} Q_{11}\left[z,\quad z^2,\quad z\frac{H}{\pi}\sin\left(\frac{\pi z}{H}\right)\right]\mathrm{d}z,$$

$$\eta_{31} = \int_{-H/2}^{H/2} Q_{55}\left(-\frac{\pi}{H}\sin\left(\frac{\pi z}{H}\right)\right)^2\mathrm{d}z,$$

$$\eta_{32} = \int_{h_{1,3}} \left(e_{15}\cos\left(\frac{\pi z_{1,3}}{h_{1,3}}\right)\cos\left(\frac{\pi z}{H}\right)\right)\mathrm{d}z,$$

$$[\eta_{33},\quad \eta_{34},\quad \eta_{35}] = \int_{-H/2}^{H/2} Q_{11}\left[\frac{H}{\pi}\sin\left(\frac{\pi z}{H}\right),\quad z\frac{H}{\pi}\sin\left(\frac{\pi z}{H}\right),\quad \left(\frac{H}{\pi}\sin\left(\frac{\pi z}{H}\right)\right)^2\right]\mathrm{d}z,$$

$$[\eta_{36},\quad \eta_{37},\quad \eta_{38}] = \int_{-H/2}^{H/2} Q_{12}\left[\frac{H}{\pi}\sin\left(\frac{\pi z}{H}\right),\quad z\frac{H}{\pi}\sin\left(\frac{\pi z}{H}\right),\quad \left(\frac{H}{\pi}\sin\left(\frac{\pi z}{H}\right)\right)^2\right]\mathrm{d}z,$$

$$\eta_{39} = \int_{h_{1,3}} \left(\frac{e_{31}\pi f(z)}{h_{1,3}}\sin\left(\frac{\pi z_{1,3}}{h_{1,3}}\right)\right)\mathrm{d}z,$$

$$[\eta_{40},\quad \eta_{41}] = \int_{-H/2}^{H/2} 2\mu l_m^2\left[\frac{H}{\pi}\sin\left(\frac{\pi z}{H}\right),\quad \left(\frac{H}{\pi}\sin\left(\frac{\pi z}{H}\right)\right)^2\right]\mathrm{d}z,$$

$$[\eta_{42},\quad \eta_{43}] = \int_{-H/2}^{H/2} 2\mu l_m^2\left[\frac{H}{\pi}\sin\left(\frac{\pi z}{H}\right)\left(-\frac{\pi}{H}\sin\left(\frac{\pi z}{H}\right)\right),\quad -\frac{\pi}{H}\sin\left(\frac{\pi z}{H}\right)\right]\mathrm{d}z,$$

$$[\eta_{44},\quad \eta_{45},\quad \eta_{46}] = \int_{-H/2}^{H/2} 2\mu l_m^2\left[\frac{H}{\pi}\sin\left(\frac{\pi z}{H}\right)\left(-\frac{\pi}{H}\sin\left(\frac{\pi z}{H}\right)\right),\quad \left(-\frac{\pi}{H}\sin\left(\frac{\pi z}{H}\right)\right)^2,\quad \left(\cos\left(\frac{\pi z}{H}\right)\right)^2\right]\mathrm{d}z,$$

$$\eta_{47} = \int_{-H/2}^{H/2} Q_{66}\left(\frac{H}{\pi}\sin\left(\frac{\pi z}{H}\right)\right)^2\mathrm{d}z,$$

$$[\eta_{48},\quad \eta_{49},\quad \eta_{50}] = \int_{h_{1,3}} \left[d_{11}\cos\left(\frac{\pi z_{1,3}}{h_{1,3}}\right)^2,\quad d_{22}\cos\left(\frac{\pi z_{1,3}}{h_{1,3}}\right)^2,\quad d_{33}\left(\frac{\pi}{h_{1,3}}\sin\left(\frac{\pi z_{1,3}}{h_{1,3}}\right)\right)^2\right]\mathrm{d}z,$$

$$[\eta_{51},\quad \eta_{52}] = \int_{h_{1,3}} \cos\left(\frac{\pi z_{1,3}}{h_{1,3}}\right)\cos\left(\frac{\pi z}{H}\right)[e_{15},\quad e_{24}]\mathrm{d}z,$$

$$[\eta_{53},\quad \eta_{54},\quad \eta_{55}] = \int_{h_{1,3}} e_{31}\frac{\pi}{h_{1,3}}\sin\left(\frac{\pi z_{1,3}}{h_{1,3}}\right)\left[1,\quad z,\quad \frac{H}{\pi}\sin\left(\frac{\pi z}{H}\right)\right]\mathrm{d}z,$$

$$[\eta_{56},\quad \eta_{57},\quad \eta_{58}] = \int_{h_{1,3}} e_{32}\frac{\pi}{h_{1,3}}\sin\left(\frac{\pi z_{1,3}}{h_{1,3}}\right)\left[1,\quad z,\quad \frac{H}{\pi}\sin\left(\frac{\pi z}{H}\right)\right]\mathrm{d}z$$

Appendix B

The arrays of stiffness matrix $[K_e]$ defined in Eq. (36) are as:

$$K_{11} = 1/8\,\frac{\eta_1 m^2\pi^4 n^2}{a^2b^2} + \frac{\eta_{13} n^2\pi^2}{b^2} + \frac{\eta_5 m^2\pi^2}{a^2} + 1/8\,\frac{\eta_1 n^4\pi^4}{b^4},$$

$$K_{12} = \frac{\eta_{13} m\pi^2 n}{ab} + \frac{\eta_8 m\pi^2 n}{ab} - 1/8\,\frac{\eta_1 m^3\pi^4 n}{a^3 b} - 1/8\,\frac{\eta_1 m\pi^4 n^3}{ab^3},$$

$$K_{13} = -2\,\frac{\eta_{14} m\pi^3 n^2}{ab^2} - \frac{\eta_9 m\pi^3 n^2}{ab^2} - \frac{\eta_6 m^3\pi^3}{a^3},$$

$$K_{14} = 1/8\,\frac{\eta_2 m^2\pi^4 n^2}{a^2b^2} + \frac{\eta_{15} n^2\pi^2}{b^2} + \frac{\eta_7 m^2\pi^2}{a^2} + 1/8\,\frac{\eta_3 n^2\pi^2}{b^2} + 1/8\,\frac{\eta_2 n^4\pi^4}{b^4},$$

$$K_{15} = \frac{\eta_{15} m\pi^2 n}{ab} + \frac{\eta_{10} m\pi^2 n}{ab} - 1/8\,\frac{\eta_2 m^3\pi^4 n}{a^3 b} - 1/8\,\frac{\eta_2 m\pi^4 n^3}{ab^3} - 1/8\,\frac{\eta_3 m\pi^2 n}{ab},$$

$$K_{16} = -\frac{\eta_{11} m\pi}{a},$$

$$K_{21} = \frac{\eta_{13} m\pi^2 n}{ab} + \frac{\eta_8 m\pi^2 n}{ab} - 1/8\,\frac{\eta_1 m^3\pi^4 n}{a^3 b} - 1/8\,\frac{\eta_1 m\pi^4 n^3}{ab^3},$$

$$K_{22} = 1/8\,\frac{\eta_1 m^4\pi^4}{a^4} + \frac{\eta_{16} n^2\pi^2}{b^2} + \frac{\eta_{13} m^2\pi^2}{a^2} + 1/8\,\frac{\eta_1 m^2\pi^4 n^2}{a^2b^2},$$

$$K_{23} = -\frac{\eta_{17} n^3\pi^3}{b^3} - \frac{\eta_9 m^2\pi^3 n}{a^2 b} - 2\,\frac{\eta_{14} m^2\pi^3 n}{a^2 b},$$

$$K_{24} = \frac{\eta_{15} m\pi^2 n}{ab} + \frac{\eta_{10} m\pi^2 n}{ab} - 1/8\,\frac{\eta_2 m^3\pi^4 n}{a^3 b} - 1/8\,\frac{\eta_2 m\pi^4 n^3}{ab^3} - 1/8\,\frac{\eta_3 m\pi^2 n}{ab},$$

$$K_{25} = 1/8\,\frac{\eta_3 m^2\pi^2}{a^2} + \frac{\eta_{15} m^2\pi^2}{a^2} + \frac{\eta_{18} n^2\pi^2}{b^2} + 1/8\,\frac{\eta_2 m^4\pi^4}{a^4} + 1/8\,\frac{\eta_2 m^2\pi^4 n^2}{a^2b^2},$$

$$K_{26} = -\frac{\eta_{19} n\pi}{b},$$

$$K_{31} = -2\,\frac{\eta_{25} m\pi^3 n^2}{ab^2} - \frac{\eta_{28} m^3\pi^3}{a^3} - \frac{\eta_{59} m\pi^3 n^2}{ab^2},$$

$$K_{32} = -\frac{\eta_{22} n^3\pi^3}{b^3} - 2\,\frac{\eta_{25} m^2\pi^3 n}{a^2 b} - \frac{\eta_{59} m^2\pi^3 n}{a^2 b},$$

$$K_{33} = 4\,\frac{\eta_{26} m^2\pi^4 n^2}{a^2b^2} + \frac{\eta_1 m^2\pi^4 n^2}{a^2b^2} + 2\,\frac{\eta_{60} m^2\pi^4 n^2}{a^2b^2} - J_2\left(-\frac{m^2\pi^2}{a^2} - \frac{n^2\pi^2}{b^2}\right) + J_1 + 1/2\,\frac{\eta_1 m^4\pi^4}{a^4} + \frac{\eta_{23} n^4\pi^4}{b^4} - \frac{Ny_0 n^2\pi^2}{b^2} - \frac{Nx_0 m^2\pi^2}{a^2} + 1/2\,\frac{\eta_1 n^4\pi^4}{b^4} + \frac{\eta_{29} m^4\pi^4}{a^4},$$

$$K_{34} = -1/4\,\frac{\eta_{21} m^3\pi^3}{a^3} - \frac{\eta_{30} m^3\pi^3}{a^3} - 2\,\frac{\eta_{27} m\pi^3 n^2}{ab^2} - 1/4\,\frac{\eta_{21} m\pi^3 n^2}{ab^2} - \frac{\eta_{61} m\pi^3 n^2}{ab^2},$$

$$K_{35} = -\frac{\eta_{24} n^3\pi^3}{b^3} - 1/4\,\frac{\eta_{21} n^3\pi^3}{b^3} - 2\,\frac{\eta_{27} m^2\pi^3 n}{a^2 b} - \frac{\eta_{61} m^2\pi^3 n}{a^2 b} - 1/4\,\frac{\eta_{21} m^2\pi^3 n}{a^2 b},$$

$$K_{36} = \frac{\eta_{12} m^2\pi^2}{a^2} + \frac{\eta_{20} n^2\pi^2}{b^2},$$

$$K_{41} = \frac{\eta_{15} n^2\pi^2}{b^2} + 1/8\,\frac{\eta_{43} n^2\pi^2}{b^2} + 1/8\,\frac{\eta_{40} n^4\pi^4}{b^4} + \frac{\eta_{33} m^2\pi^2}{a^2} + 1/8\,\frac{\eta_{40} m^2\pi^4 n^2}{a^2b^2},$$

$$K_{42} = -1/8\,\frac{\eta_{43} m\pi^2 n}{ab} - 1/8\,\frac{\eta_{40} m\pi^4 n^3}{ab^3} + \frac{\eta_{15} m\pi^2 n}{ab} + \frac{\eta_{36} m\pi^2 n}{ab} - 1/8\,\frac{\eta_{40} m^3\pi^4 n}{a^3 b},$$

$$K_{43} = -1/4\,\frac{\eta_{21} m^3\pi^3}{a^3} - \frac{\eta_{34} m^3\pi^3}{a^3} - 1/4\,\frac{\eta_{21} m\pi^3 n^2}{ab^2} - \frac{\eta_{37} m\pi^3 n^2}{ab^2} - 2\,\frac{\eta_{27} m\pi^3 n^2}{ab^2},$$

$$K_{44} = 1/8\,\frac{\eta_{44} n^2\pi^2}{b^2} + 1/8\,\frac{\eta_{42} n^2\pi^2}{b^2} + 1/8\,\frac{\eta_{41} n^4\pi^4}{b^4} + 1/8\,\frac{\eta_{46} m^2\pi^2}{a^2} + 1/2\,\frac{\eta_{46} n^2\pi^2}{b^2} + \frac{\eta_{47} n^2\pi^2}{b^2} + \frac{\eta_{35} m^2\pi^2}{a^2} + 1/8\,\frac{\eta_{41} m^2\pi^4 n^2}{a^2b^2} + \eta_{31} + \eta_{45}/8,$$

$$K_{45} = \frac{\eta_{38} m\pi^2 n}{ab} - 1/8\frac{\eta_{44} m\pi^2 n}{ab} - 1/8\frac{\eta_{41} m\pi^4 n^3}{ab^3} - 3/8\frac{\eta_{46} m\pi^2 n}{ab} + \frac{\eta_{47} m\pi^2 n}{ab} - 1/8\frac{\eta_{42} m\pi^2 n}{ab} - 1/8\frac{\eta_{41} m^3\pi^4 n}{a^3 b},$$

$$K_{46} = -\frac{\eta_{32} m\pi}{a} - \frac{\eta_{39} m\pi}{a},$$

$$K_{51} = -1/8\frac{\eta_{43} m\pi^2 n}{ab} - 1/8\frac{\eta_{40} m\pi^4 n^3}{ab^3} + \frac{\eta_{15} m\pi^2 n}{ab} + \frac{\eta_{36} m\pi^2 n}{ab} - 1/8\frac{\eta_{40} m^3\pi^4 n}{a^3 b},$$

$$K_{52} = \frac{\eta_{15} m^2\pi^2}{a^2} + 1/8\frac{\eta_{43} m^2\pi^2}{a^2} + 1/8\frac{\eta_{40} m^4\pi^4}{a^4} + \frac{\eta_{36} n^2\pi^2}{b^2} + 1/8\frac{\eta_{40} m^2\pi^4 n^2}{a^2 b^2},$$

$$K_{53} = -1/4\frac{\eta_{21} n^3\pi^3}{b^3} - \frac{\eta_{37} n^3\pi^3}{b^3} - \frac{\eta_{37} m^2\pi^3 n}{a^2 b} - 2\frac{\eta_{27} m^2\pi^3 n}{a^2 b} - 1/4\frac{\eta_{21} m^2\pi^3 n}{a^2 b},$$

$$K_{54} = \frac{\eta_{38} m\pi^2 n}{ab} - 1/8\frac{\eta_{44} m\pi^2 n}{ab} - 1/8\frac{\eta_{41} m\pi^4 n^3}{ab^3} - 3/8\frac{\eta_{46} m\pi^2 n}{ab} + \frac{\eta_{47} m\pi^2 n}{ab} - 1/8\frac{\eta_{42} m\pi^2 n}{ab} - 1/8\frac{\eta_{41} m^3\pi^4 n}{a^3 b},$$

$$K_{55} = 1/8\frac{\eta_{44} m^2\pi^2}{a^2} + \frac{\eta_{47} m^2\pi^2}{a^2} + 1/2\frac{\eta_{46} m^2\pi^2}{a^2} + 1/8\frac{\eta_{42} m^2\pi^2}{a^2} + 1/8\frac{\eta_{46} n^2\pi^2}{b^2} + 1/8\frac{\eta_{41} m^4\pi^4}{a^4} + \frac{\eta_{38} n^2\pi^2}{b^2} + 1/8\frac{\eta_{41} m^2\pi^4 n^2}{a^2 b^2} + \eta_{45}/8 + \eta_{33},$$

$$K_{56} = -\frac{\eta_{34} n\pi}{b} - \frac{\eta_{30} n\pi}{b},$$

$$K_{61} = -\frac{\eta_{53} m\pi}{a},$$

$$K_{62} = -\frac{\eta_{56} n\pi}{b},$$

$$K_{63} = \frac{\eta_{54} m^2\pi^2}{a^2} + \frac{\eta_{57} n^2\pi^2}{b^2},$$

$$K_{64} = -\frac{\eta_{51} m\pi}{a} - \frac{\eta_{55} m\pi}{a},$$

$$K_{65} = -\frac{\eta_{52} n\pi}{b} - \frac{\eta_{58} n\pi}{b},$$

$$K_{66} = -\frac{\eta_{48} m^2\pi^2}{a^2} - \frac{\eta_{50} n^2\pi^2}{b^2} - \eta_{49}$$

References

[1] Soleimani-Javid Z, Arshid E, Khorasani M, Amir S, Tounsi A. Size-dependent flexoelectricity-based vibration characteristics of honeycomb sandwich plates with various boundary conditions. Adv Nano Res 2021;10:460. https://doi.org/10.12989/ANR.2021.10.5.449.

[2] Khorasani M, Soleimani-Javid Z, Arshid E, Lampani L, Civalek Ö. Thermo-elastic buckling of honeycomb micro plates integrated with FG-GNPs reinforced Epoxy skins with stretching effect. Compos Struct 2021;258:113430.

[3] Gibson LJ, Ashby MF, Schajer GS, Robertson CI. Mechanics of two-dimensional cellular materials. Proc R Soc London, Ser A Math Phys Sci 1982;382:25–42. https://doi.org/10.1098/rspa.1982.0087.

[4] Minghui F, Jiuren Y. Equivalent elastic parameters of the honeycomb core. Acta Mech Sin 1999;31:113–8.

[5] Yu SD, Cleghorn WL. Free flexural vibration analysis of symmetric honeycomb panels. J Sound Vib 2005;284:189–204. https://doi.org/10.1016/j.jsv.2004.06.028.

[6] Maheri MR, Adams RD. Steady-state flexural vibration damping of honeycomb sandwich beams. Compos Sci Technol 1994;52:333–47. https://doi.org/10.1016/0266-3538(94)90168-6.

[7] Ruzzene M. Vibration and sound radiation of sandwich beams with honeycomb truss core. J Sound Vib 2004;277:741–63. https://doi.org/10.1016/j.jsv.2003.09.026.

[8] Kargar J, Ghorbanpour Arani A, Arshid E, Irani RM. Vibration analysis of spherical sandwich panels with MR fluids core and magneto-electro-elastic face sheets resting on orthotropic viscoelastic foundation. Struct Eng Mech 2021;78:572. https://doi.org/10.12989/SEM.2021.78.5.557.

[9] Sahmani S, Aghdam MM. Axial postbuckling analysis of multilayer functionally graded composite nanoplates reinforced with GPLs based on nonlocal strain gradient theory. Eur Phys J Plus 2017;132:1–17. https://doi.org/10.1140/epjp/i2017-11773-4.

[10] Shen H-S, Xiang Y, Lin F, Hui D. Buckling and postbuckling of functionally graded graphene-reinforced composite laminated plates in thermal environments. Compos Part B Eng 2017;119:67–78. https://doi.org/10.1016/J.COMPOSITESB.2017.03.020.

[11] Amir S, Arshid E, Khoddami Maraghi Z, Loghman A, Ghorbanpour AA. Vibration analysis of magnetorheological fluid circular sandwich plates with magnetostrictive facesheets exposed to monotonic magnetic field located on visco-Pasternak substrate. JVC/J Vib Control 2020;26:1523–37. https://doi.org/10.1177/1077546319899203.

[12] Xiao X, Bu G, Ou Z, Li Z. Nonlinear in-plane instability of the confined FGP arches with nanocomposites reinforcement under radially-directed uniform pressure. Eng Struct 2022;252:113670. https://doi.org/10.1016/J.ENGSTRUCT.2021.113670.

[13] Ma X, Quan W, Dong Z, Dong Y, Si C. Dynamic response analysis of vehicle and asphalt pavement coupled system with the excitation of road surface unevenness. Appl Math Model 2022;104:421–38. https://doi.org/10.1016/J.APM.2021.12.005.

[14] Dai G, Zhang W. Cell size effects for vibration analysis and design of sandwich beams. Acta Mech Sin Xuebao 2009;25:353–65. https://doi.org/10.1007/s10409-009-0230-1.

[15] Hajmohammad MH, Kolahchi R, Zarei MS, Nouri AH. Dynamic response of auxetic honeycomb plates integrated with agglomerated CNT-reinforced face sheets subjected to blast load based on visco-sinusoidal theory. Int J Mech Sci 2019; 153–154:391–401. https://doi.org/10.1016/j.ijmecsci.2019.02.008.
[16] Cheng S, Qiao P, Chen F, Fan W, Zhu Z. Free vibration analysis of fiber-reinforced polymer honeycomb sandwich beams with a refined sandwich beam theory. J Sandw Struct Mater 2016;18:242–60. https://doi.org/10.1177/1099636215619841.
[17] Subramani M, Arumugam AB, Ramamoorthy M. Vibration analysis of carbon fiber reinforced laminated composite skin with glass honeycomb sandwich beam using HSDT. Period Polytech Mech Eng 2017;61:213–24. https://doi.org/10.3311/PPme.9747.
[18] Yongqiang L, Dawei Z. Free flexural vibration analysis of symmetric rectangular honeycomb panels using the improved Reddy's third-order plate theory. Compos Struct 2009;88:33–9. https://doi.org/10.1016/j.compstruct.2008.03.033.
[19] de Souza Eloy F, Gomes GF, Ancelotti AC, da Cunha SS, Bombard AJF, Junqueira DM. Experimental dynamic analysis of composite sandwich beams with magnetorheological honeycomb core. Eng Struct 2018;176:231–42.
[20] Li Y, Zhou M, Wang T, Zhang Y. Nonlinear primary resonance with internal resonances of the symmetric rectangular honeycomb sandwich panels with simply supported along all four edges. Thin-Walled Struct 2020;147:106480. https://doi.org/10.1016/j.tws.2019.106480.
[21] Wang Y-J, Zhang Z-J, Xue X-M, Zhang L. Free vibration analysis of composite sandwich panels with hierarchical honeycomb sandwich core. Thin-Walled Struct 2019;145:106425.
[22] Malgaca L, Uyar M. Hybrid vibration control of a flexible composite box cross-sectional manipulator with piezoelectric actuators. Compos Part B Eng 2019;176: 107278. https://doi.org/10.1016/j.compositesb.2019.107278.
[23] Zhou H, Xu C, Lu C, Jiang X, Zhang Z, Wang J, et al. Investigation of transient magnetoelectric response of magnetostrictive/piezoelectric composite applicable for lightning current sensing. Sens Actuat A Phys 2021;329. https://doi.org/10.1016/J.SNA.2021.112789.
[24] Lin HG, Cao DQ, Xu YQ. Vibration, buckling and aeroelastic analyses of functionally graded multilayer graphene-nanoplatelets-reinforced composite plates embedded in piezoelectric layers. Int J Appl Mech 2018;10:1850023. https://doi.org/10.1142/S1758825118500230.
[25] Mao JJ, Zhang W. Buckling and post-buckling analyses of functionally graded graphene reinforced piezoelectric plate subjected to electric potential and axial forces. Compos Struct 2019;216:392–405. https://doi.org/10.1016/j.compstruct.2019.02.095.
[26] Wu CP, Chen H. Exact solutions of free vibration of simply supported functionally graded piezoelectric sandwich cylinders using a modified Pagano method. J Sandw Struct Mater 2013;15:229–57. https://doi.org/10.1177/1099636212471357.
[27] Li J, Li F, Narita Y. Active control of thermal buckling and vibration for a sandwich composite laminated plate with piezoelectric fiber-reinforced composite actuator facesheets. J Sandw Struct Mater 2019;21:2563–81. https://doi.org/10.1177/1099636218783168.
[28] Soleimani-Javid Z, Arshid E, Amir S, Bodaghi M. On the higher-order thermal vibrations of FG saturated porous cylindrical micro-shells integrated with nanocomposite skins in viscoelastic medium. Def Technol 2021. https://doi.org/10.1016/J.DT.2021.07.007.
[29] Arshid E, Amir S, Loghman A. Bending and buckling behaviors of heterogeneous temperature-dependent micro annular/circular porous sandwich plates integrated by FGPEM nano-composite layers. J Sandwich Struct Mater 2021;23(8):3836–77.
[30] Jiang L, Wang Y, Wang X, Ning F, Wen S, Zhou Y, et al. Electrohydrodynamic printing of a dielectric elastomer actuator and its application in tunable lenses. Compos Part A Appl Sci Manuf 2021;147:106461.
[31] Hu L-B, Huang X-Y, Zhang S, Chen X, Dong X-H, Jin He, et al. MoO3 structures transition from nanoflowers to nanorods and their sensing performances. J Mater Sci Mater Electron 2021;32(19):23728–36.
[32] Lu Z-Q, Zhang F-Y, Fu H-L, Ding Hu, Chen L-Q. Rotational nonlinear double-beam energy harvesting. Smart Mater Struct 2022;31(2):025020.
[33] Li J, Xue Y, Li F, Narita Y. Active vibration control of functionally graded piezoelectric material plate. Compos Struct 2019;207:509–18. https://doi.org/10.1016/j.compstruct.2018.09.053.
[34] Arshid E, Khorshidvand AR. Free vibration analysis of saturated porous FG circular plates integrated with piezoelectric actuators via differential quadrature method. Thin-Walled Struct 2018;125:220–33. https://doi.org/10.1016/j.tws.2018.01.007.
[35] Duc ND, Cong PH, Quang VD. Nonlinear dynamic and vibration analysis of piezoelectric eccentrically stiffened FGM plates in thermal environment. Int J Mech Sci 2016;115–116:711–22. https://doi.org/10.1016/j.ijmecsci.2016.07.010.
[36] Keleshteri MM, Asadi H, Wang Q. Large amplitude vibration of FG-CNT reinforced composite annular plates with integrated piezoelectric layers on elastic foundation. Thin-Walled Struct 2017;120:203–14. https://doi.org/10.1016/j.tws.2017.08.035.
[37] Abad F, Rouzegar J. An exact spectral element method for free vibration analysis of FG plate integrated with piezoelectric layers. Compos Struct 2017;180:696–708. https://doi.org/10.1016/j.compstruct.2017.08.030.
[38] Zhao X, Zhu WD, Li YH. Analytical solutions of nonlocal coupled thermoelastic forced vibrations of micro-/nano-beams by means of Green's functions. J Sound Vib 2020;481:115407.
[39] Zhao X, Chen B, Li YH, Zhu WD, Nkiegaing FJ, Shao YB. Forced vibration analysis of Timoshenko double-beam system under compressive axial load by means of Green's functions. J Sound Vib 2020;464:115001.
[40] Mirjavadi SS, Rabby S, Shafiei N, Afshari BM, Kazemi M. On size-dependent free vibration and thermal buckling of axially functionally graded nanobeams in thermal environment. Appl Phys A 2017 1235 2017;123:1–10. doi:10.1007/S00339-017-0918-1.
[41] Zhang Z, Liu M, Zhou M, Chen J. Dynamic reliability analysis of nonlinear structures using a Duffing-system-based equivalent nonlinear system method. Int J Approx Reason 2020;126:84–97. https://doi.org/10.1016/j.ijar.2020.08.006.
[42] Zhu P, Lei ZX, Liew KM. Static and free vibration analyses of carbon nanotube-reinforced composite plates using finite element method with first order shear deformation plate theory. Compos Struct 2012;94:1450–60. https://doi.org/10.1016/j.compstruct.2011.11.010.
[43] Selim BA, Zhang LW, Liew KM. Vibration analysis of CNT reinforced functionally graded composite plates in a thermal environment based on Reddy's higher-order shear deformation theory. Compos Struct 2016;156:276–90. https://doi.org/10.1016/j.compstruct.2015.10.026.
[44] Yang J, Chen D, Kitipornchai S. Buckling and free vibration analyses of functionally graded graphene reinforced porous nanocomposite plates based on Chebyshev-Ritz method. Compos Struct 2018;193:281–94. https://doi.org/10.1016/J.COMPSTRUCT.2018.03.090.
[45] Zhong R, Wang Q, Tang J, Shuai C, Qin B. Vibration analysis of functionally graded carbon nanotube reinforced composites (FG-CNTRC) circular, annular and sector plates. Compos Struct 2018;194:49–67. https://doi.org/10.1016/j.compstruct.2018.03.104.
[46] Arshid E, Khorshidvand AR, Khorsandijou SM. The effect of porosity on free vibration of SPFG circular plates resting on visco-Pasternak elastic foundation based on CPT. FSDT and TSDT Struct Eng Mech 2019;70:97–112. https://doi.org/10.12989/sem.2019.70.1.097.
[47] Gao N, Tang L, Deng J, Lu K, Hou H, Chen K. Design, fabrication and sound absorption test of composite porous metamaterial with embedding I-plates into porous polyurethane sponge. Appl Acoust 2021;175:107845. https://doi.org/10.1016/j.apacoust.2020.107845.
[48] Eyvazian A, Taghizadeh SA, Hamouda AM, Tarlochan F, Moeinifard M, Gobbi M. Buckling and crushing behavior of foam-core hybrid composite sandwich columns under quasi-static edgewise compression: Https://DoiOrg/101177/1099636219894665 2019. doi:10.1177/1099636219894665.
[49] Talebizadehsardari P, Eyvazian A, Asmael M, Karami B, Shahsavari D, Mahani RB. Static bending analysis of functionally graded polymer composite curved beams reinforced with carbon nanotubes. Thin-Walled Struct 2020;157:107139. https://doi.org/10.1016/j.tws.2020.107139.
[50] Talebizadehsardari P, Eyvazian A, Musharavati F, Mahani RB, Sebaey TA. Elastic wave characteristics of graphene reinforced polymer nanocomposite curved beams including thickness stretching effect. Polym (Basel) 2020;12:2194. https://doi.org/10.3390/polym12102194.
[51] Bouazza M, Becheri T, Boucheta A, Benseddiq N. Bending behavior of laminated composite plates using the refined four-variable theory and the finite element method. Earthquakes Struct 2019;17:257–70. https://doi.org/10.12989/eas.2019.17.3.257.
[52] Mohammadimehr M, Arshid E, Alhosseini SMAR, Amir S, Arani MRG. Free vibration analysis of thick cylindrical MEE composite shells reinforced CNTs with temperature-dependent properties resting on viscoelastic foundation. Struct Eng Mech 2019;70:683–702. https://doi.org/10.12989/sem.2019.70.6.683.
[53] Eyvazian A, Shahsavari D, Karami B. On the dynamic of graphene reinforced nanocomposite cylindrical shells subjected to a moving harmonic load. Int J Eng Sci 2020;154:103339. https://doi.org/10.1016/j.ijengsci.2020.103339.
[54] Amir S, Arshid E, Rasti-Alhosseini SMA, Loghman A. Quasi-3D tangential shear deformation theory for size-dependent free vibration analysis of three-layered FG porous micro rectangular plate integrated by nano-composite faces in hygrothermal environment. J Therm Stress 2020;43(2):133–56.
[55] Eyvazian A, Musharavati F, Tarlochan F, Pasharavesh A, Rajak DK, Husain MB, et al. Free vibration of FG-GPLRC conical panel on elastic foundation. Struct Eng Mech 2020;75:1–18. https://doi.org/10.12989/SEM.2020.75.1.001.
[56] Zhang C, Wang L, Eyvazian A, Khan A, Sebaey TA. Analytical solution for static and dynamic analysis of FGP cylinders integrated with FG-GPLs patches exposed to longitudinal magnetic field. Eng Comput 2021:1–19. https://doi.org/10.1007/s00366-021-01361-3.
[57] Becheri T, Amara K, Bouazza M, Benseddiq N. Buckling of symmetrically laminated plates using nth-order shear deformation theory with curvature effects. Steel Compos Struct 2016;21:1347–68. https://doi.org/10.12989/scs.2016.21.6.1347.
[58] Bouazza M, Zenkour AM. Hygro-thermo-mechanical buckling of laminated beam using hyperbolic refined shear deformation theory. Compos Struct 2020;252: 112689. https://doi.org/10.1016/j.compstruct.2020.112689.
[59] Bouazza M, Benseddiq N. Analytical modeling for the thermoelastic buckling behavior of functionally graded rectangular plates using hyperbolic shear deformation theory under thermal loadings. Multidiscip Model Mater Struct 2015; 11:558–78. https://doi.org/10.1108/MMMS-02-2015-0008.
[60] Arshid E, Khorasani M, Soleimani-Javid Z, Amir S, Tounsi A. Porosity-dependent vibration analysis of FG microplates embedded by polymeric nanocomposite patches considering hygrothermal effect via an innovative plate theory. Eng Comput 2021:1–22. https://doi.org/10.1007/s00366-021-01382-y.
[61] Eringen AC. On differential equations of nonlocal elasticity and solutions of screw dislocation and surface waves. J Appl Phys 1983;54(9):4703–10.
[62] Eringen AC. Nonlocal continuum field theories. Springer Science & Business Media; 2002.
[63] Amir S, Bidgoli EMR, Arshid E. Size-dependent vibration analysis of a three-layered porous rectangular nano plate with piezo-electromagnetic face sheets subjected to pre loads based on SSDT. Mech Adv Mater Struct 2020;27:605–19. https://doi.org/10.1080/15376494.2018.1487612.

[64] Shahverdi H, Barati MR. Vibration analysis of porous functionally graded nanoplates. Int J Eng Sci 2017;120:82–99. https://doi.org/10.1016/J.IJENGSCI.2017.06.008.

[65] Ellali M, Amara K, Bouazza M, Bourada F. The buckling of piezoelectric plates on pasternak elastic foundation using higher-order shear deformation plate theories. Smart Struct Syst 2018;21:113–22. https://doi.org/10.12989/sss.2018.21.1.113.

[66] Bouazza M, Zenkour AM, Benseddiq N. Closed-from solutions for thermal buckling analyses of advanced nanoplates according to a hyperbolic four-variable refined theory with small-scale effects. Acta Mech 2018;229:2251–65. https://doi.org/10.1007/s00707-017-2097-8.

[67] Arshid E, Arshid H, Amir S, Mousavi SB. Free vibration and buckling analyses of FG porous sandwich curved microbeams in thermal environment under magnetic field based on modified couple stress theory. Arch Civ Mech Eng 2021;21:6. https://doi.org/10.1007/s43452-020-00150-x.

[68] Arshid E, Amir S, Loghman A. Thermal buckling analysis of FG graphene nanoplatelets reinforced porous nanocomposite MCST-based annular/circular microplates. Aerosp Sci Technol 2021;111:106561.

[69] Mousavi SB, Amir S, Jafari A, Arshid E. Analytical solution for analyzing initial curvature effect on vibrational behavior of PM beams integrated with FGP layers based on trigonometric theories. Adv Nano Res 2021;10:251. https://doi.org/10.12989/ANR.2021.10.3.235.

[70] Khorasani M, Soleimani-Javid Z, Arshid E, Amir S, Civalek Ö. Vibration analysis of graphene nanoplatelets' reinforced composite plates integrated by piezo-electromagnetic patches on the piezo-electromagnetic media. Waves Random Complex Medium 2021:1–31. https://doi.org/10.1080/17455030.2021.1956017.

[71] Farzam A, Hassani B. Isogeometric analysis of in-plane functionally graded porous microplates using modified couple stress theory. Aerosp Sci Technol 2019;91:508–24. https://doi.org/10.1016/j.ast.2019.05.012.

[72] Le TC, Tran LV, Vu-Huu T, Nguyen-Xuan H, Abdel-Wahab M. Size-dependent nonlinear analysis and damping responses of FG-CNTRC micro-plates. Comput Methods Appl Mech Eng 2019;353:253–76. https://doi.org/10.1016/j.cma.2019.05.002.

[73] Zhang B, Li H, Kong L, Shen H, Zhang X. Size-dependent vibration and stability of moderately thick functionally graded micro-plates using a differential quadrature-based geometric mapping scheme. Eng Anal Bound Elem 2019;108:339–65. https://doi.org/10.1016/j.enganabound.2019.08.014.

[74] Li Q, Wu D, Gao W, Tin-Loi F. Size-dependent instability of organic solar cell resting on Winkler-Pasternak elastic foundation based on the modified strain gradient theory. Int J Mech Sci 2020;177:105306. https://doi.org/10.1016/j.ijmecsci.2019.105306.

[75] Arefi M, Mohammad-Rezaei Bidgoli E, Rabczuk T. Effect of various characteristics of graphene nanoplatelets on thermal buckling behavior of FGRC micro plate based on MCST. Eur J Mech A/Solids 2019;77:103802. https://doi.org/10.1016/j.euromechsol.2019.103802.

[76] Torabi K, Afshari H, Aboutalebi FH. Vibration and flutter analyses of cantilever trapezoidal honeycomb sandwich plates. Vibration and Flutter Analyses of Cantilever trapezoidal honeycomb sandwich plates 2019;21(8):2887–920.

[77] Sobhy M. Differential quadrature method for magneto-hygrothermal bending of functionally graded graphene/Al sandwich-curved beams with honeycomb core via a new higher-order theory. J Sandw Struct Mater 2021;23(5):1662–700.

[78] Arshid E, Amir S. Size-dependent vibration analysis of fluid-infiltrated porous curved microbeams integrated with reinforced functionally graded graphene platelets face sheets considering thickness stretching effect. Proc Inst Mech Eng, Part L: J Mater: Des Appl 2021;235(5):1077–99.

[79] Amir S, Arshid E, Ghorbanpour Arani MR. Size-dependent magneto-electro-elastic vibration analysis of FG saturated porous annular/ circular micro sandwich plates embedded with nano-composite face sheets subjected to multi-physical pre loads. Smart Struct Syst 2019;23:429–47. https://doi.org/10.12989/sss.2019.23.5.429.

[80] Arshid E, Kiani A, Amir S. Magneto-electro-elastic vibration of moderately thick FG annular plates subjected to multi physical loads in thermal environment using GDQ method by considering neutral surface. Proc Inst Mech Eng Part L J Mater Des Appl 2019;233:2140–59. https://doi.org/10.1177/1464420719832626.

[81] Sobhy M. Magneto-electro-thermal bending of FG-graphene reinforced polymer doubly-curved shallow shells with piezoelectromagnetic faces. Compos Struct 2018;203:844–60. https://doi.org/10.1016/j.compstruct.2018.07.056.

[82] Sobhy M. Piezoelectric bending of GPL-reinforced annular and circular sandwich nanoplates with FG porous core integrated with sensor and actuator using DQM. Arch Civ Mech Eng 2021 212 2021;21:1–18. doi:10.1007/S43452-021-00231-5.

[83] Arshid E, Kiani A, Amir S, Zarghami DM. Asymmetric free vibration analysis of first-order shear deformable functionally graded magneto-electro-thermo-elastic circular plates. Proc Inst Mech Eng Part C J Mech Eng Sci 2019;233:5659–75. https://doi.org/10.1177/0954406219850598.

[84] Brush DO, Almroth BO, Hutchinson JW. Buckling of bars, plates, and shells. J Appl Mech 1975;42:911.

[85] Arshid E, Amir S, Loghman A. Static and dynamic analyses of FG-GNPs reinforced porous nanocomposite annular micro-plates based on MSGT. Int J Mech Sci 2020;180:105656. https://doi.org/10.1016/j.ijmecsci.2020.105656.

[86] Abazid MA, Sobhy M. Thermo-electro-mechanical bending of FG piezoelectric microplates on Pasternak foundation based on a four-variable plate model and the modified couple stress theory. Microsyst Technol 2018;24:1227–45. https://doi.org/10.1007/s00542-017-3492-8.

[87] Singh SJ, Harsha SP. Analysis of porosity effect on free vibration and buckling responses for sandwich sigmoid function based functionally graded material plate resting on Pasternak foundation using Galerkin Vlasov's method. J Sandwich Struct Mater 2021;23(5):1717–60.

[88] Zenkour AM, Sobhy M. Nonlocal piezo-hygrothermal analysis for vibration characteristics of a piezoelectric Kelvin-Voigt viscoelastic nanoplate embedded in a viscoelastic medium. Acta Mech 2018;229:3–19. https://doi.org/10.1007/s00707-017-1920-6.

[89] Alhaifi K, Arshid E, Khorshidvand AR. Large deflection analysis of functionally graded saturated porous rectangular plates on nonlinear elastic foundation via GDQM. Steel Compos Struct 2021;39:809. https://doi.org/10.12989/SCS.2021.39.6.795.

[90] Amir S, Arshid E, Khoddami MZ. Free vibration analysis of magneto-rheological smart annular three-layered plates subjected to magnetic field in viscoelastic medium. Smart Struct Syst 2020;25:581–92. https://doi.org/10.12989/sss.2020.25.5.581.

[91] Mahani RB, Eyvazian A, Musharavati F, Sebaey TA, Talebizadehsardari P. Thermal buckling of laminated Nano-Composite conical shell reinforced with graphene platelets. Thin-Walled Struct 2020;155:106913. https://doi.org/10.1016/j.tws.2020.106913.

[92] Khorasani M, Eyvazian A, Karbon M, Tounsi A, Lampani L, Sebaey TA, et al. Magneto-electro-elastic vibration analysis of modified couple stress-based three-layered micro rectangular plates exposed to multi-physical fields considering the flexoelectricity effects. Smart Struct Syst 2020;26:331. https://doi.org/10.12989/SSS.2020.26.3.331.

[93] Ebrahimi F, Barati MR. Temperature distribution effects on buckling behavior of smart heterogeneous nanosize plates based on nonlocal four-variable refined plate theory. Int J Smart Nano Mater 2016;7:119–43. https://doi.org/10.1080/19475411.2016.1223203.

[94] Zenkour AM, Aljadani MH. Porosity effect on thermal buckling behavior of actuated functionally graded piezoelectric nanoplates. Eur J Mech A/Solids 2019;78:103835. https://doi.org/10.1016/j.euromechsol.2019.103835.

[95] He L, Lou J, Zhang E, Wang Y, Bai Y. A size-dependent four variable refined plate model for functionally graded microplates based on modified couple stress theory. Compos Struct 2015;130:107–15. https://doi.org/10.1016/j.compstruct.2015.04.033.

[96] Jamalpoor A, Ahmadi-Savadkoohi A, Hosseini-Hashemi Sh. Free vibration and biaxial buckling analysis of magneto-electro-elastic microplate resting on visco-Pasternak substrate via modified strain gradient theory. Smart Mater Struct 2016;25(10):105035.